Droplet Wettability and Impact Behavior on High-Temperature Microstructured Surfaces
(高温微細構造表面上での液滴の濡れ性と衝突挙動)

January, 2019
Precision Machinery Engineering Major
Graduate School of Science and Technology
Doctoral Course
Nihon University
HAN　YUXUAN

Contents

Chapter 1: Introduction: Wettability on the Microstructured Surface

Chapter 2: Profile Characterization and Temperature Effect on the Wettability of Microstructured Surfaces

Chapter 3: High temperature wettability on Microstructured Superhydrophobic Surface

Chapter 4: Thermodynamic Analysis on Wetting Behavior of the Microstructured Surfaces

Chapter 5: The Droplet Rebound Temperature on the Microstructure surfaces

Chapter 6: Outlook

Chapter 1

Introduction: Wettability on the Microstructured Surface

Abstract

In this thesis, the wetting behaviors and droplet impact on the heated microstructured surface were investigated. In this chapter, the concepts of wettability and a short description of its history and growth were given. The fabricate technology used in this thesis was detailed. The investigation on the static wettability and dynamic impact in this thesis could render an interesting candidate for application in microfluidics.

1.1 Wetting phenomenon in nature

The topic of wetting has received tremendous interest from both fundamental and applied points of view. It plays an important role in many industrial processes, such as oil recovery, lubrication, liquid coating, printing, and spray quenching [1–4].

Nature is a great genius to design the world with mystical principles, wetting is one of the omnipresent phenomena governed via the natural laws. Wetting is a common occurrence that many lives take advantage of in order to adapt to their living environment, such as the self-cleaning property of lotus leaves [5], the superior water-walking ability of water striders [6], the directional adhesion of butterfly wings [5,7], the antifogging functionality of mosquito eyes [8], the water collection of the Namib Desert beetle and spider silk [9,10], the submarine self-cleaning ability of fish scale [11], and the use of plastron respiration for underwater breathing [12]. There are a few examples presented in Fig.1.1.

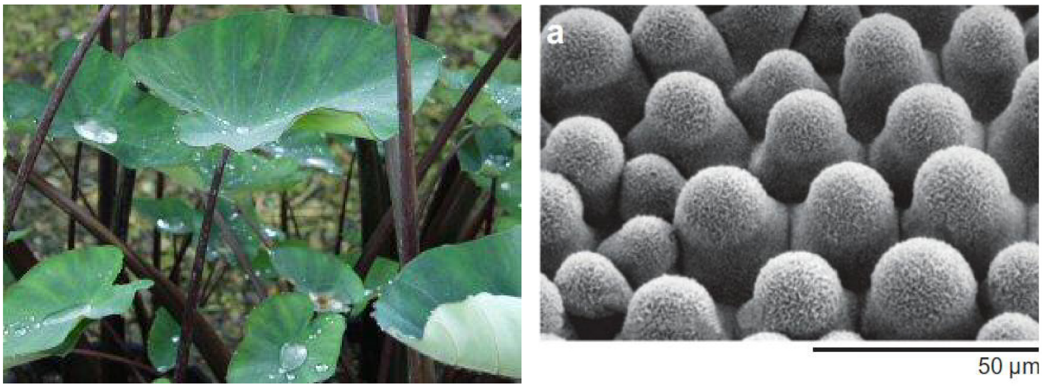

(a) Leaf of Colocasia esculenta.

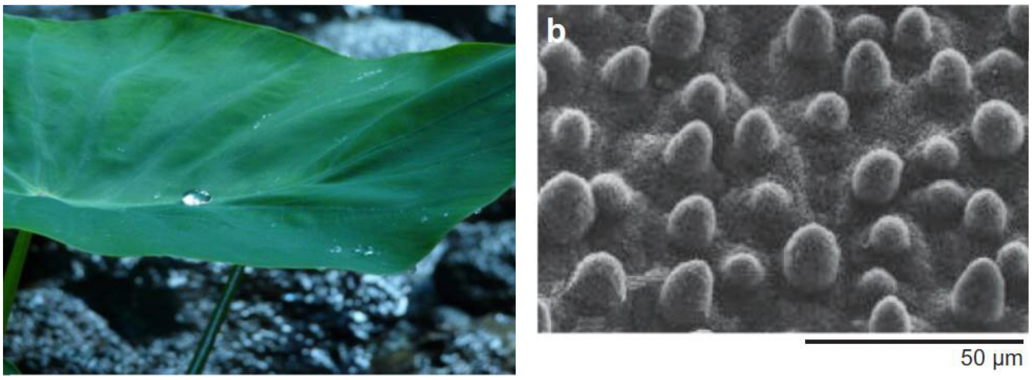

(b) Lotus leaf

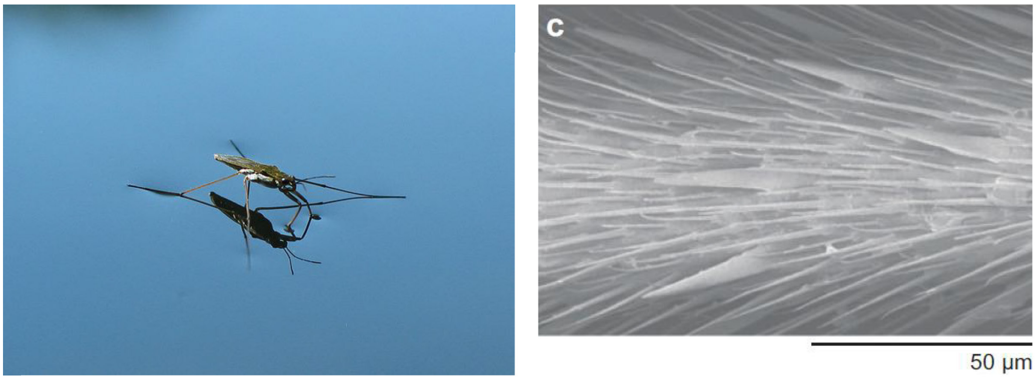

(c) Leg of a water strider

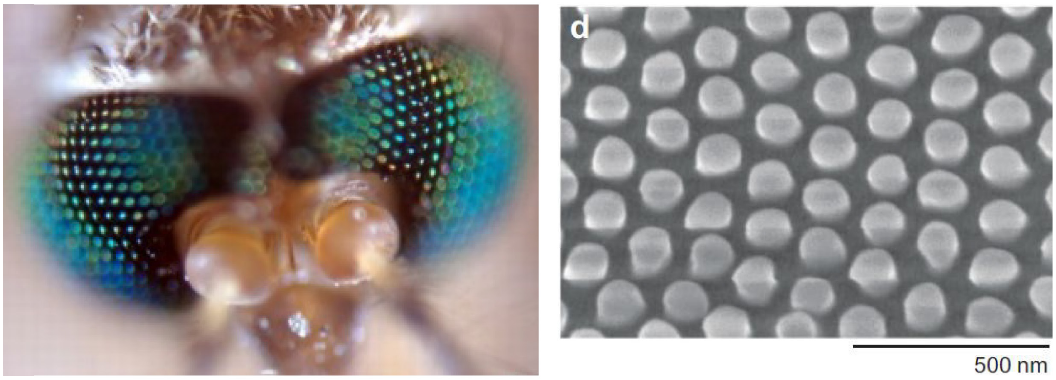

(d) Surface of a mosquito eye

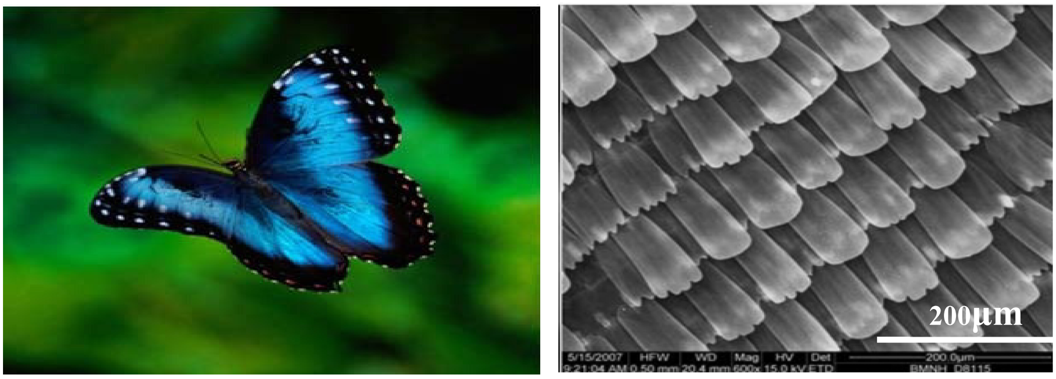

(e) Surface of butterfly wings

Fig.1.1 Some natural superhydrophobic materials, and their revealed by SEM[13,14]

Excited by these special properties of the natural creatures, the superhydrophobic/superoleophobic surface based on bionics has become a research hotspot. The large area superhydrophobic/superoleophobic surface has been produced extremely important application in industrial and agricultural production and people's daily life. For example, using a special process made of hydrophobic and oleophobic clothes not only stain fabrics to achieve long-term clean, but also effectively reduce the breeding of germs, therefore, people's daily lives has been brought great convenience; the non-stick pans made of PTFE with a special combination of lotus leaf microstructures have been a necessity in every kitchen due to their oleophobic property. Non-stick pans are not only easier to clean, but also greatly reduce the amount of used cooking oil and the cooking time. The application of self-cleaning materials to the curtain wall of the building surface can eliminate the need for manual and frequent cleaning, save a lot of cost and reduce safety hazards; for underwater transportation vehicles or underwater submarines, can reduce the resistance of the water, increases the speed of navigation and saves fuel. It can be seen that both daily life and national construction and even aerospace, super-hydrophobic/super-oleophobic surfaces have extremely wide application.

Human beings are always keen on understanding and imitating nature to improve our own society. From the pioneering work of Young

[15] and Laplace 200 years ago, many efforts have been devoted to explore the mechanism of wetting. The surface energy theory has well explained those static wetting phenomena mentioned above. Specifically, the value of contact angle among three phases is determined by Young-equation and the interface's shape follows the Young-Laplace formula.

In recent years, there has been an increasing interest in the study of superhydrophobic surfaces, due to their potential applications in, for example, self-cleaning, nanofluidics, and electrowetting [16–20].

Usually superhydrophobic surface can be obtained by two ways:

One is to use chemical treatment to minimize the surface free energy of the material; the other is to increase the surface roughness of the hydrophobic material to increase the contact angle, or to combine the two to produce low surface energy and high roughness. More specifically, in the current research, there are mainly the following methods for making super-hydrophobic surfaces: Researchers created varies methods to fabricate the hierarchical structures such as lithography[21], electro deposition[22], chemical deposition[23], sputtering[24], anodization[25], and ultrafast laser surface texturing[26] on silicon[27], polymer[26, 28] and metals[25, 29]. Superhydrophobic surface, typically an effect enhanced by surface roughness, has recently attracted great attention because of the easy fabrication of microstructured surfaces with superhydrophobicity.

Many researchers create the various microstructures surfaces with special wettability.[11, 16, 19, 20, 30-33].

Quanshui Zheng [34] reported the superhydrophobic silicon surfaces were fabricated by Si ICP etching technology. The profile effect on the contact angle on the micro-pillar surface was analyzed. Tommaso Baldacchini [35] reported superhydrophobic silicon surfaces were prepared using high energy femtosecond pulsed laser processing techniques. Didem Oner [36] reported that a series of microstructures with different structural parameters are prepared on the surface of silicon by reactive ion etching. The surface is treated by silanization solution to obtain superhydrophobic properties of more than 170°. Changing the structural parameters for testing and comparison, the optimized parameters are obtained, and the water droplets are easily rolled on the surface. Hong Zhao [37] reported that the masked and Bosch etching method is used to etch a regular laminated trench structure on a silicon wafer, and the low surface energy modification is performed by using fluorosilane. The obtained grating microstructure silicon surface has superhydrophobic and self-cleaning performance.

Researchers created many special wettability surfaces. However, few researchers investigate the temperature affect coupled with microstructure. But surface wettability at non-ambient temperature was of great importance in many industrial processes, including water transportation and metal processing.[38, 39] Therefore, of temperature depended wettability on microstructured surfaces is important and imperative.

In this thesis, we will focus on investigation of the temperature and profile effect on the hydrophobic and superhydrophobic micro-pillar structured surfaces and the dynamic droplet impact behaviors on the heated micro-pillar structured surface.

1.2 Contact angle and hysteresis

Wettability studies usually involve the measurement of contact angles as the primary data, which indicates the degree of wetting when a solid and liquid interact. Small contact angles (<90°) correspond to high wettability, while large contact angles (>90°) correspond to low wettability (as shown in Fig.1.2).

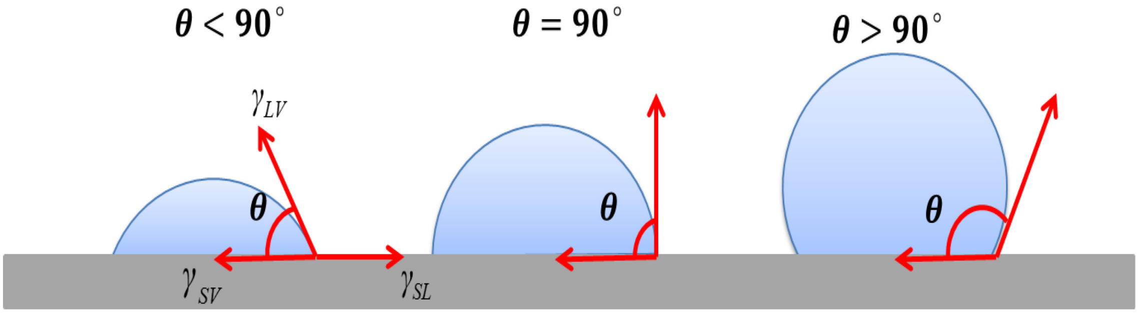

Fig.1.2. Illustration of contact angles on a smooth homogeneous solid surface

Surface tension

Although liquid is easily deformed by external forces, the droplets are always tending to be a sphere somehow. This is because of surface tension, which pulls the surface layer to make the exposed surface area as minimal as possible. This phenomenon can be viewed in the terms of energy: a molecule surrounded by neighbors on all sides is much more stable than the molecule that misses some neighbors. The force balance and unbalance are showed in Fig.1.3.

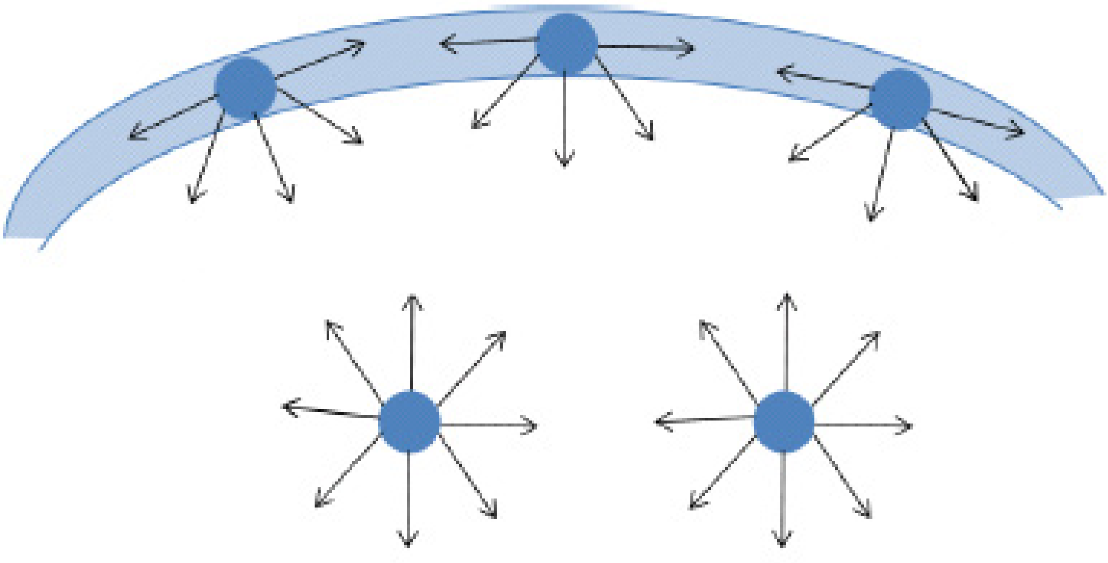

Fig.1.3. Diagram of the forces on molecules inside the liquid and on the interface

Thus, the interior molecules has lower energy than the molecules at the interface between liquid and air. In order to minimize energy state and stabilize the whole system, the surface area is kept as small as possible, resulting in the spherical shape.

Equilibrium state and contact angle

Consider a liquid drop resting on a flat, horizontal solid surface (Fig.1.2). The contact angle is defined as the angle formed by the intersection of the liquid-solid interface and the liquid-vapor interface (geometrically acquired by applying a tangent line from the contact point along the liquid-vapor interface in the droplet profile). The interface where solid, liquid, and vapor co-exist is referred to as the “three phase contact line”. Fig.1.2 showed that a small contact angle was observed when the liquid spreads on the surface, while a large contact angle is observed when the liquid beads on the surface. More specifically, a contact angle less than 90° indicates that wetting of the surface is favorable, and the fluid will spread over a large area on the surface; while contact angles greater than 90° generally means that wetting of the surface is unfavorable so the fluid will minimize its contact with the surface and form a compact liquid droplet.

For wetting, the discussion of the surface energy situation is more complicated than the free surface due to a third phase introduced. In this case, there are three kinds of interfaces: liquid-vapor (γ_{LV}), solid- vapor (γ_{SV}) and solid-liquid (γ_{SL}). When a droplet stops on a flat substrate, it reaches its equilibrium state. Young’s equation[15] describes the equilibrium state in terms of force balance (as shown in Fig.1.2).

$$\cos\theta = (\gamma_{SV}-\gamma_{SL})/\gamma_{LV} \tag{1.1}$$

Nevertheless, Young’s equation is only suitable for the surface which was ideal; that is to say, smooth and chemically homogeneous.

Contact angle hysteresis

From Young's equation applied to a specific liquid-solid system, three thermodynamic parameters γ_{LV} , γ_{SV}, and γ_{SL} determine a single and unique contact angle θ. In practice, however, there exist many metastable states of a droplet on a solid, and the observed contact angles are usually not equal to θ. The phenomenon of wetting is more than just a static state. The liquid moves to expose its fresh surface and to wet the fresh surface of the solid in turn. The measurement of a single static contact angle to characterize wetting behavior is no longer adequate.

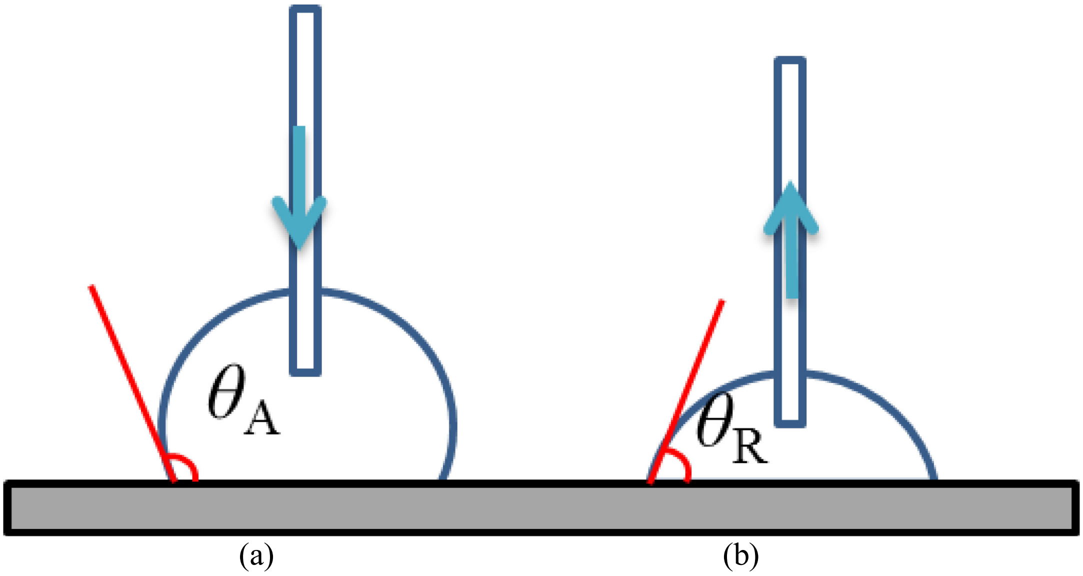

Fig.1. 4. (a) Advancing and (b) receding contact angles measurement using Increase/Decrease liquid Method

If the three-phase contact line was in actual motion, the contact angle produced was called a "dynamic" contact angle. In particular, the contact angles formed by expanding and contracting the liquid were referred to as the advancing contact angle θ_A and the receding contact angle θ_R, respectively (Fig.1.4). These angles fall within a range, with the advancing angles approaching a maximum value, and the receding angles approaching a minimum value [40, 41]. The difference between the advancing angle and the receding angle is called the contact angle hysteresis (CAH):

$$\theta_H=\theta_A-\theta_R \tag{1.2}$$

1.3 Wetting behavior on the microstructured surface

In practice, solids are usually rough and heterogeneous, which therefore calls for more understanding of the influence of such surface characteristics on wetting and spreading. So far there are two standard models illustrating how the roughness or defects affect wetting properties: Wenzel's model and Cassie-Baxter model.

Wenzel's model

In 1936, R. N. Wenzel reported a model [42] describing the influence of the roughness on wetting when all the surfaces are wet by fluid (Fig.1.5). In this model, it is assumed that the local contact angle θ is given by Young's equation and the surface is rough but chemically homogeneous. When the roughness scale is much smaller than the droplet size, the apparent contact angle θ_a can be derived in the view of energy change as below. Considering a tiny displacement *dx* of the contact line in a direction of droplet spreading, the surface energies of the system changes as

$$dE=r(\gamma_{SL}-\gamma_{SV})dx+\gamma_{LV}dx\cos\theta_a \tag{1.3}$$

where r is the measure of roughness of the solid. In order to get the equilibrium state, dE is set as zero, leading to Wenzel's relation:

$$\cos\theta_w = r\cos\theta \tag{1.4}$$

where θ_w is the contact angle of droplet to the non-composite state where water penetrates into the gap space when a droplet on a rough surface.

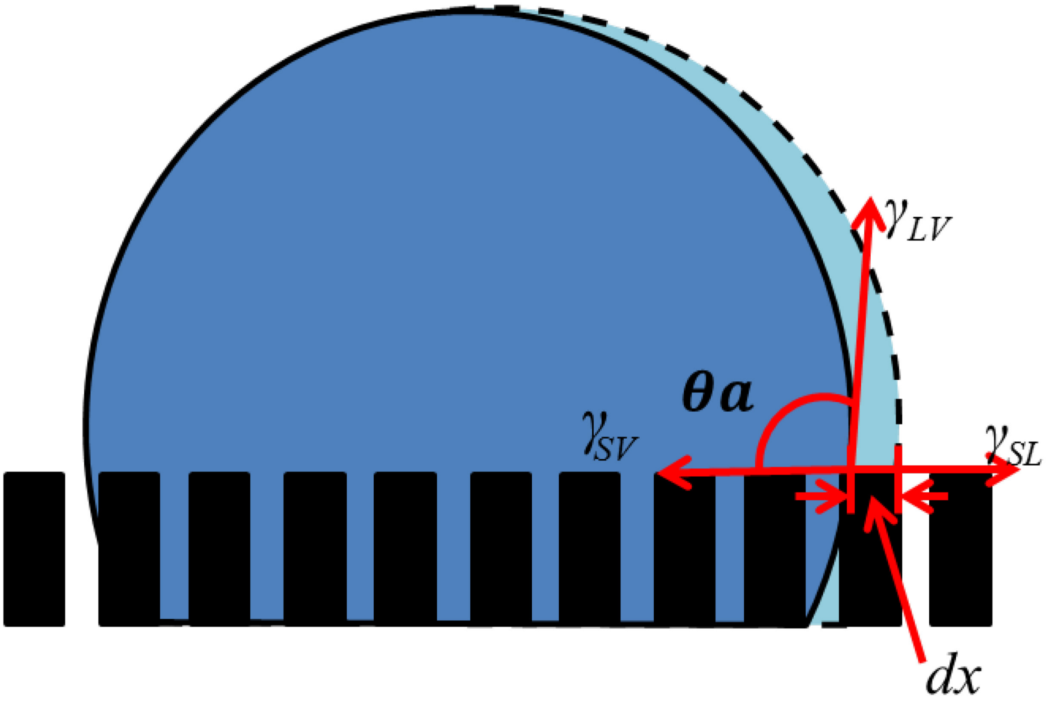

Fig.1.5. Wenzel wetting state on solid

Cassie-Baxter model

When the surface is made from or covered by two types of substances, Cassie-Baxter model [43] is applied to predict the contact angle on this composite substrate (Fig.1.6). There are several assumptions for the model to be applicable. Firstly, the surface is planar and each species is characterized by contact angle, which θ_1 is for material 1 and θ_2 for material 2. Secondly, the area fraction of each material is denoted as f_1 and f_2 for material 1and 2 respectively ($f_1 + f_2$=1). Thirdly, the individual areas are much smaller than the size of droplet. Under this condition, the apparent contact angle can also be calculated by the energy variation relation.

$$dE = f_1 (\gamma_{SL1}-\gamma_{SV1})dx + f_2(\gamma_{SL2}-\gamma_{SV2})dx + \gamma_{LV}dx\cos\theta_a \qquad (1.5)$$

The minimum of *dE*, which is zero, defines equilibrium. By substituting Young's equation into Eq. (1.5), Cassie-Baxter relation can be written as below

$$\cos\theta_a = f_1 \cos\theta_1 + f_2 \cos\theta_2 \qquad (1.6)$$

Specifically, if one of the substances was air, the contact angle was 180°, leading to the equation given as

$$\cos\theta_c = f_1 (\cos\theta + 1) - 1 \qquad (1.7)$$

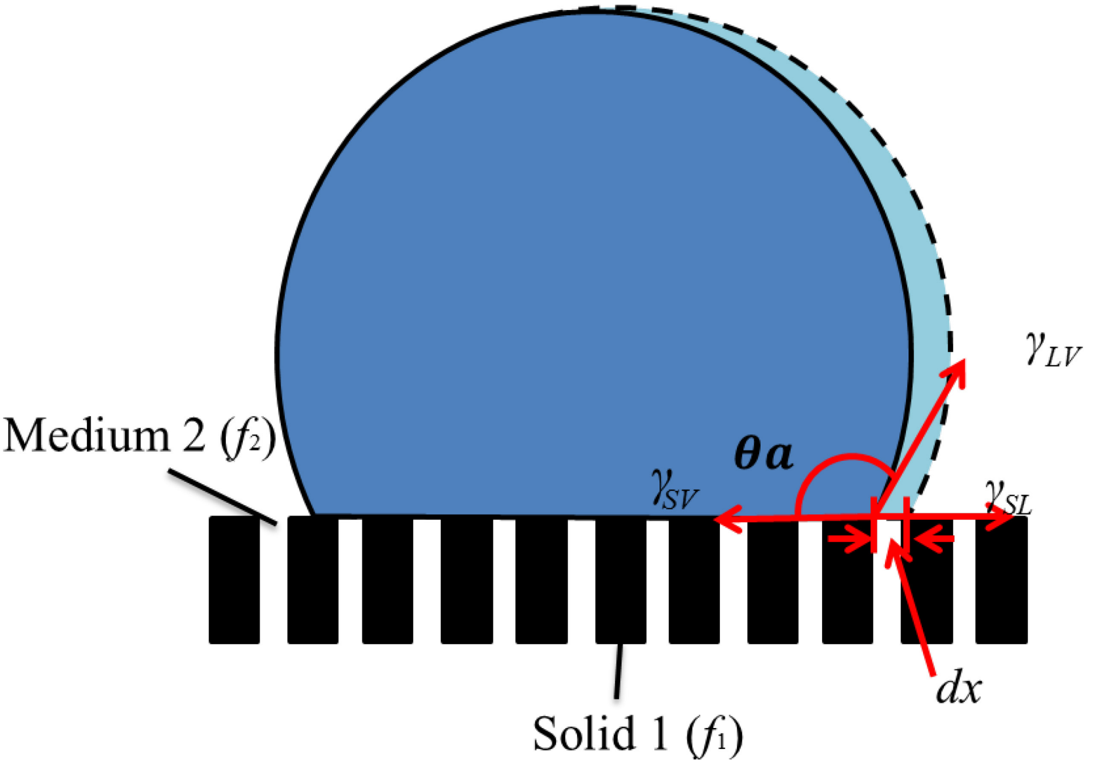

Fig.1.6. Cassie-Baxter wetting state

1.4 Creation of the special wettability surface

The extraordinary water repellency showed by superhydrophobic surface could be attributed to the combination of biomimetic micro-nano hierarchical structures and low surface energies. A. Marmur puts the Wenzel and Cassie-Baxter equations into proper mathematical-thermodynamic perspective and defines the conditions for determining the transition between the homogeneous and heterogeneous wetting regimes [44]. As we introduced before, varies methods have been developed to create the hierarchical structures. Among of them, microfabrication recently attracted great attention because of the easy fabrication of microstructured surfaces with special wettability.

Microfabrication is the technology to fabricate miniature devices, which are made up of components generally ranging from 1 to 100um [45]. Recently in the MEMS field, burgeoning research efforts have been made to develop the fabrication methods so that obtaining my desired microstructures with accurate size on the silicon wafer is no longer a big problem. In this research, the photolithography and Si inductively coupled plasma (ICP) etching techniques are employed to fabricate the micro-pillar structured surfaces.

a) Photolithography process

A single iteration of photolithography combines several steps in sequence. The basic steps are photoresist spin-coated, exposure, developing, and photoresist remove.

The Si surface is spin-coated with a particular kind of polymer, which can change its molecular properties after exposition to an electromagnetic radiation. A viscous, liquid solution of photoresist (S1815) is dispensed onto the wafer, and the wafer is spun rapidly to produce a uniformly thick layer. The spin coating runs at two steps, 500 rpm for 5 seconds, and 3000rpm for 30 seconds. The spin coating process results in a uniform thin layer, usually with uniformity of within 5 to 10 nanometers. This uniformity can be explained by detailed fluid-mechanical modeling, which shows that the resist moves much faster at the top of the layer than at the bottom, where viscous forces bind the resist to the wafer surface. Thus, the top layer of resist is quickly ejected from the wafer's edge while the bottom layer still creeps slowly radially along the wafer. In this way, any bump or ridge of resist is removed, leaving a very flat layer. Final thickness is also determined by the evaporation of liquid solvents from the resist.

The photoresist-coated wafer is then prebaked to drive off excess photoresist solvent, at 90 °C for 20 minutes in a bake oven. The final photoresist layer was approximate 1.5 microns thick.

After prebaking, the photoresist is exposed to a pattern of intense light. The optical lithography uses ultraviolet light that wave length is 486 nm (hg-g line). Since the photoresist used in this study is a positive photoresist, the photoresist becomes soluble in the basic developer (MF-319) that contained tetramethylammonium hydroxide (TMAH) when exposed. The micro-pillar structure was optically defined on the photoresist using a mask.

b) Silicon etching

The silicon anisotropic etching using inductively coupled plasma (ICP) (STS MUC21) was performed using the Bosch process as described elsewhere [46]. The Bosh process employs alternative SF6 silicon etching and polymer deposition processes using C4F8 plasmas for the anisotropic etching of silicon.

For the ICP etching, the operating is that the Fluorine ions are accelerated in the electric field. Cause them to collide into the surface of the sample. A hard mask (aluminum layer or photoresist layer) is used to protect certain areas from etching, exposing only the areas desired to be etched. Another mechanism is sidewall passivation: deposition of a chemically inert passivation layer CxFy functional groups (C4F8 source gas yields a substance similar to Teflon) condensate on the sidewalls, and protect them from lateral etching. As a combination of these processes deep vertical structures can be made (see in Fig. 1.7).

The etching ions are accelerated into the etching region, where they combine with silicon and then are dispersed. Because the electric field accelerated ions toward the surface, the etching caused by these ions is much more dominant than the etching of radicals - ions traveling in varied directions, and the sidewall passivation protect the sidewall well, so the etching are anisotropic.

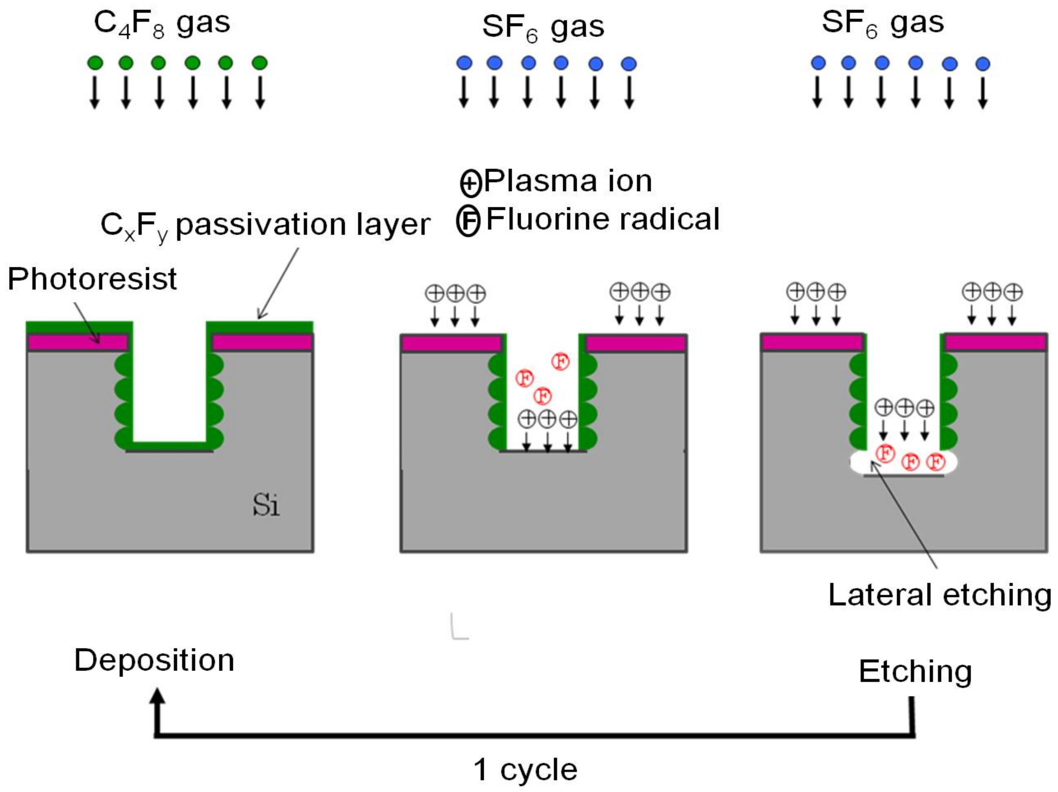

Fig.1.7. Schematic of ICP etching process

1.5 Wettability measurements

1) Static contact angle measurements

Gas-liquid–solid interfaces of droplets on a micro-structured surface can be continuous in the single-phase regime. The temperature-dependent wettability of single-phase regime droplets was characterized using contact angle measurements. Contact angle (CA) measurements were assessed at different temperatures with the KRUSS temperature controlled chamber TC21 for the temperature control of samples and Droplet Sharp Analyzer DSA25 for a contact angle measurement (as shown in Fig 1.8), which places a water droplet of 10 µL on the micro-structured substrate.

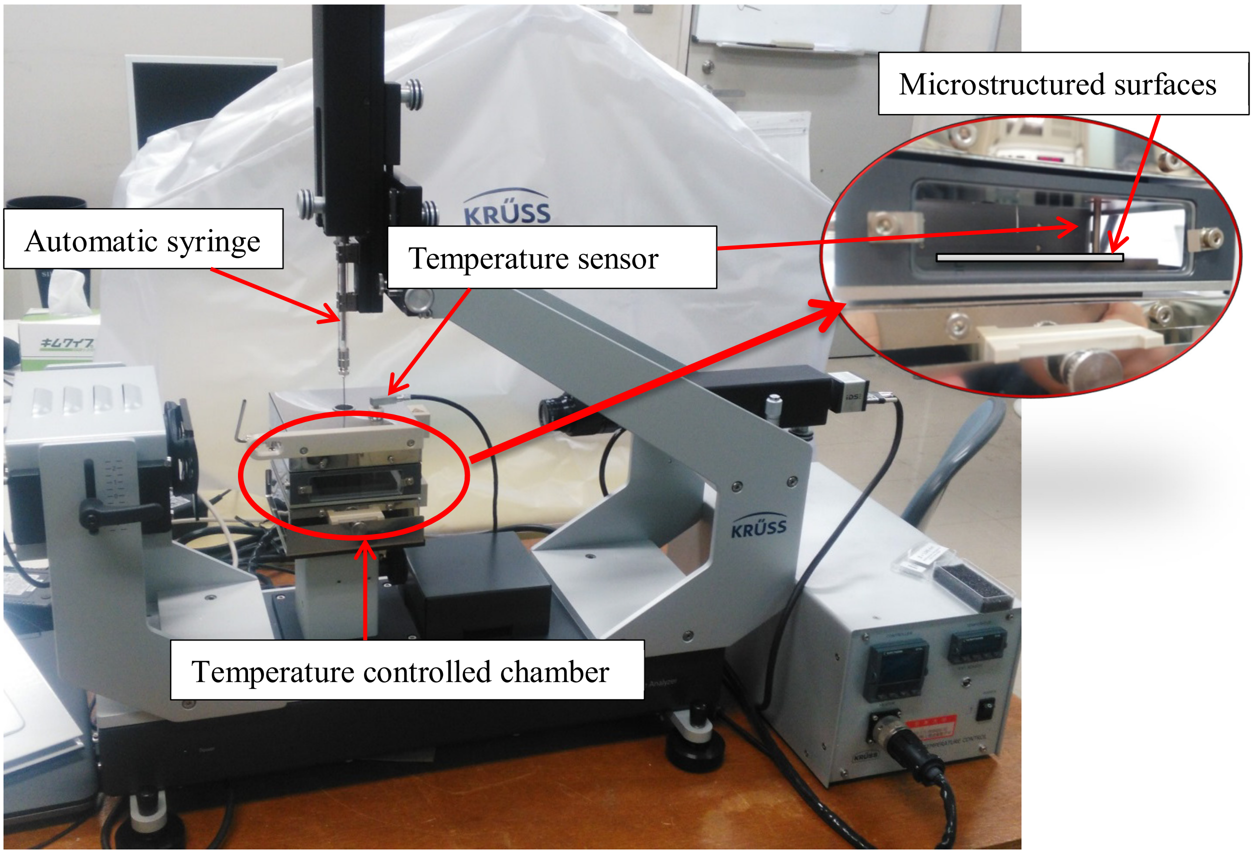

Fig 1.8 Contact angle measurement equipment (KRUSS DSA25 & TC21)

The temperature controlled chamber TC21 enables liquid and solid surfaces to be analyzed at temperatures up to 400 °C. The shown temperature is the sensor temperature on the top side of the microstructured surfaces. The target temperature is easy to specify and reliably achieved at defined heating rates. The chamber's excellent insulation ensures stable equilibrium during the measurement. An accurate temperature sensor is located on the top of surfaces to measure the actual temperature. With the help of the temperature sensor, the current value is recorded by the software together with the contact angle.

The used DI water (18.2 MΩ•cm) was purified in a DI water system. The fabricated Si wafer was cleared by the RCA cleaning process before taking the contact angle measurement. The 10 μL DI water droplets were produced by the automatic controlled syringe. This automatic syringe was used to generate droplets with an injection rate of 0.15mL/min to reduce the inertial effects. The temperature of the droplet is 28 °C (room temperature). All the static contact angles are measured three times using the polynomial fitting method on each surface. In order to stabilize the surface temperatures, the interval between each measurement is 5 minutes at same surface temperature and 10 minutes when the surface temperatures are changed.

2) Droplet rebounded observing

For the droplet impact behaviors observing, the surface temperature and the water spreading or rebounding are recorded with a precise thermo sensor and a CCD, respectively. The injector was kept 20 mm higher than the heating surfaces to preserve the drop from heat. A 10 μL DI water droplet was pushed out. The water droplet was well preserved before coming into contact with the high-temperature surfaces.

A Digital camera with high-speed model (Nikon1 J5) was employed to record the spreading and rebounding processes of impacting droplets from the side. From the side-view recording of each impact experiment, the droplet impact is measured.

1.6 Scope of this thesis

All the knowledge and models above shed light on the dominant mechanism of wetting, while the general theory still faces a great challenge for further insight. Moreover, the developing history is also a sign that the effects of topography is frequently overlooked, although we have learned that the geometry on substrates can strongly modify the properties of static wetting such as Cassie wetting state. However, few researchers investigate the surface temperature and topography effect on the wetting behaviors simultaneously.

Since temperature depended wettability on microstructured surfaces is important and imperative, we will investigate the temperature depended wettability of the hydrophobic and superhydrophobic micro-pillar structured surfaces and the dynamic droplet impact behaviors on the heated micro-pillar structured surface to obtaining controllable wettability on micro-structured surfaces at different surface temperature.

The wettability of surfaces is determined by surface temperature and roughness. In this thesis we study the static wetting properties at different temperatures and dynamic droplet impact on heated microstructured surface.

In Chapter 1 an introduction to the wettability and microfabrication, the main subjects in this thesis, is provided. The study of wettability on the solid surfaces is placed in a historic perspective and the fabrication process of the microstructures surfaces was shortly introduced.

In Chapter 2 Si wafers with various structures were fabricated to investigate wettability at different temperatures. Three shapes with micro-pillar structured surfaces were designed and fabricated. Pillar-structured surfaces were fabricated by photolithography and ICP etching. The temperature-dependent wettability of single-phase regime droplets was characterized using contact angle measurements. The wetting behavior of a water droplet was observed.

Chapter 3 detailed the wettability of superhydrophobic surfaces at non-ambient temperature, especially at high temperature (30 to 90°C). In this chapter, Silicon wafers with various structures were fabricated to create superhydrophobic surfaces for investigating wettability at different temperatures. Four shapes micro-pillar structured surfaces were designed and fabricated by photolithography and ICP etching. The temperature-dependent wettability of single-phase regime droplets was characterized using contact angle measurements on these surfaces. The surface temperature and pillar parameters driven Cassie-Baxter to Wenzel wetting transition are reported on superhydrophobic surfaces. The wetting behavior of a water droplet was observed to be different on the surfaces, and the wetting transition from Cassie-Baxter state to Wenzel state occurred at 70℃ on a special micro-pillar surface .

Chapter 4 focused on the thermodynamic mechanisms of superhydrophobicity affected by surface roughness. In this chapter, a 3-D square pillar-textured surface model was chosen to investigate the thermodynamic mechanism responsible for contact angle (CA), and free energy barrier (FEB). The effects of pillar width, space between pillars and pillar height on CA and FEB were obtained, and the calculated results are essentially consistent with the results of experimental measurement. The present approach could provide a theoretical guidance for designing superhydrophobic surfaces.

Droplet impact experiments described in Chapter 5 on superheated silicon microstructured surfaces showed that the dynamic droplet rebound temperature, T_r. Two series of microstructured silicon surfaces which was decorated by micro-pillars whose pillar width, space between pillars and pillar height can be adjusted independently were fabricated. These surfaces possessed a hydrophobic/superhydrophobic property. The dynamic behavior of water droplets impacting these structured surfaces was examined using a high-speed camera. Experimental results validated that the difference in the droplet rebound temperature was subjected to the solid fraction referred to as the ratio of the actual area contacting with the liquid to its projected area on the textured surface. Because the mechanism by which the residual liquid film emerges on the pillars' tops can essentially be ascribed to the pinch-off of the liquid threads.

The microstructure on the solid surface affects the wettability surface, and the surfaces temperature also affects the wettability. The combination of these factors has brought many challenges to in-depth research, and we have been able to design more functional surfaces such as superhydrophobic surfaces to reduce flow resistance, wettability gradient surfaces to achieve self-driving of liquid droplets, separation and detection of substances on microfluidic surfaces for microfluidics. This thesis explores the interaction mechanism between solid and liquid by studying the special phenomena of droplets on different microstructures with difference temperature by experimental test and theoretical analysis. This study may provide theoretical guidance for future research on micro-heat exchanger, microfluidic, micro-separator and the engine design.

Chapter 2

Profile Characterization and Temperature Effect on the Wettability of Micro-structured Surfaces

Abstract

In the nature world wetting is a common phenomenon. The effect of surface morphology and temperature effect on the wetting behavior at different temperature (30 °C to 90 °C) was an important research that had never been studied systematically. In this research, it was studied and investigated by using contact angle measurements. Three shapes of micro-pillar structured surfaces were designed and fabricated by photolithography and ICP etching to measure the contact angles. The wetting behavior of the water droplet was observed and the regular patterns were concluded at the end.

2.1. Introduction

There are lots of wetting phenomenon in our environment including the plants and living beings. They have their special characteristics to protect themselves and adapt to the circumambient surroundings [47-51]. The mosquito eyes which have special nanometer structure can resist the wetness of fogging outside [50]. Also, the lotus leaves have fuzz like micro structure which can cause the droplet rolling down, so that it has self-cleaning property. It is important on the research of wetting to inhibit corrosion and enhance the coefficient of utilization on material [5].

The studies in controlling the surface texture and properties become much more important since wenzel effect which was reported on surface wettability of roughness [42]. The researchers are doing the research on modifying the surface roughness to enhance the surface wetting. So far, lots of researchers are doing the research focus on the wetting influence of micro structured surfaces [52], but the complexity influence including the temperature and micro-structured surface influence hasn't been discussed yet. The combination of temperature effects and micro-structure influence had been researched in this thesis.

There are two kinds of states when the droplets drip on the micro-structured surface [32]. They are Wenzel state (non-composite state) (Fig.2.1(a)) and Cassie-Baxter state (composite state) (Fig.2.1(b)). Wenzel state is the surface completely covered with droplet and no air between the liquid and solid. In Wenzel's proposal, it was described when the micro-structured surface is completely wetting the droplet contact angle is influenced by the increase of the wetted area. Cassie-Baxter state is the droplet contact part of the solid and the air is left between the solid and liquid. The micro-structured surface including the hydrophilic [33] and hydrophobic [53, 54] become much more important in the research of wetting.

On the high temperature (30 °C to 90 °C) the wettability is much important in the industry process [55]. There are lots of influence in surface wettability such as the nucleate boiling based on the lyophilic micro-structured surface leads high critical heat flux [56], the hot water repellent in super-hydrophobic surface [57], wetting transition on hydrophobic microstructured-surface during evaporation [58–60], the fabrication of wetting-controllable thermally responsive materials [61, 62], low temperature heat exchange on hydrophobic surfaces [63] and so on. It is important in water transportation and metal processing in industrial processes especially at high temperature (30 °C to 90 °C) [38]. The theory and applications of droplet wetting behavior on hot surfaces in the solid–liquid heat transfer system become much more important [64].

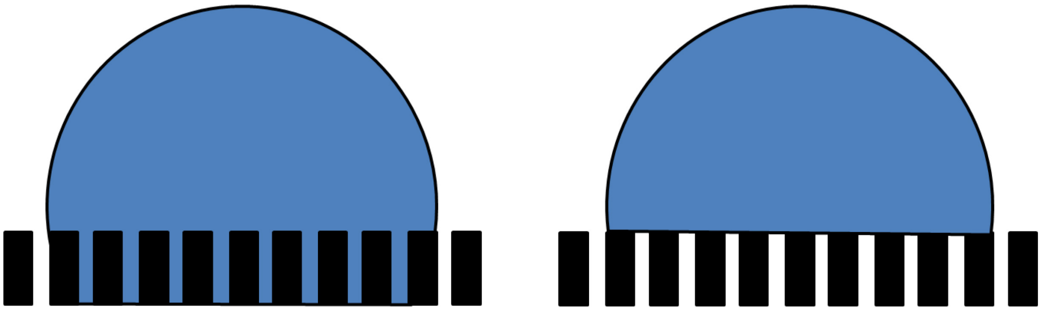

(a) Wenzel state (b) Cassie-Baxter state

Fig.2.1. States of droplets on the micro-structured surface.

So far, there is not a systematically description on wetting of temperature effect and micro-structured surface. In this research, three kinds of micro-structured surfaces were designed to research the surface wetting behavior in different temperatures from 30 °C to 90 °C. Photolithography and ICP etching were used to fabricate the silicon wafer. The characteristics of wetting with various micro-structured surfaces in different temperatures were researched and studied.

2.2. Theoretical Analysis

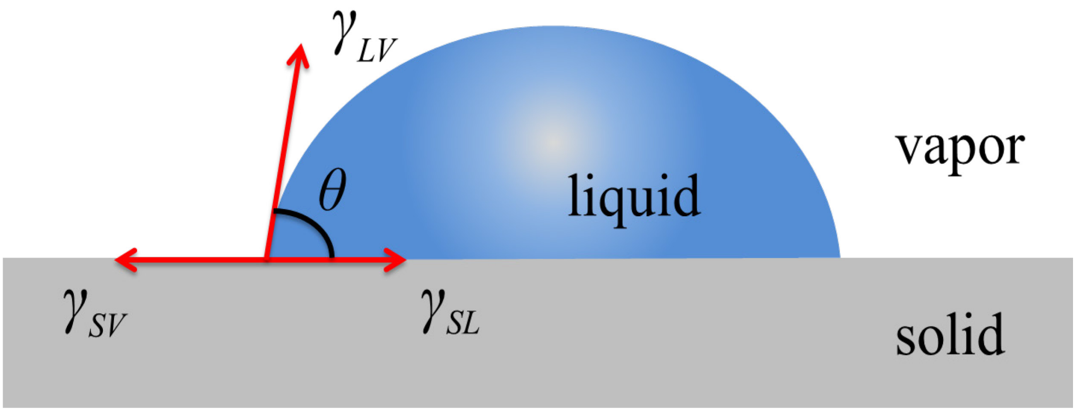

Fig.2.2. Illustration of the contact angle.

The Young equation [15] showed the relationship of the contact angle

θ on a smooth surface.

$$\cos\theta=（\gamma_{SV}-\gamma_{SL}）/\gamma_{LV} \tag{2.1}$$

In the equation, γ_{SV} is the surface tension coefficient on solid-vapor interface. γ_{SL} is surface tension coefficient on solid-liquid interface. γ_{LV} is surface tension coefficient on liquid-vapor interface。

The contact angle θ has the relation with the droplet state both the Wenzel state and Cassie-Baxter state. The equation of contact angle θ was described by Cassie and Baxter [43] as follows.

$$\cos\theta_c=（\gamma^*_{SV}-\gamma^*_{SL}）/\gamma_{LV} \tag{2.2}$$

In this equation:

$\gamma^*_{SV}=f\gamma_{SV}$; $\gamma^*_{SL}=(1-f)\gamma_{LV}+f\gamma_{SL}$. f is the area fraction.

There is another model and equation to describe the contact angle θ on a rough surface as there are three-phase contact line tension on the liquid-vapor-solid phase boundary [65-67]. In this equation, λ is the line tension and K is the influence coefficient of scale effect.

$$\cos\theta_c^*=-1+(1+\cos\theta)(1 - -\lambda/(K(1+\cos\theta)\gamma_{LV}))f \tag{2.3}$$

where λ is the line tension and K is the influence coefficient of scale effect.

2.3. Experiments

2.3.1. Fabrication of Micro-Structured Surfaces

In this research, three shapes of micro-pillar structured surfaces were designed and fabricated to investigate the wettability in different temperatures from 30 °C to 90 °C. The pillar-structured surfaces were fabricated by photolithography and inductively coupled plasma (ICP) etching. These micro-pillars were uniformly distributed in a rectangular grid on a glass mask with different values of the area fraction f.

During the fabrication, The Silicon wafer ((100), 4 Inch, 400μm thick, p-type) were used. Firstly, clear and dry the wafer in the clean room and then coated with positive photoresist (S1805) by a spin-coater. Next, transfer the required pattern from the mask to the photoresist layer by UV exposure. Then the photoresist was partly removed in the developer. Finally, the ICP etcher was used to etch the uncovered Si wafer to fabricate the roughness pattern on it. Then clear away the residual photoresist by the acetone. The etching experiments were performed in the STS ICP system.

In the designing, three shapes of micro-pillars are square pillars, triangle pillars and hexagon pillars. The side length of the square and triangle pillars were 10 μm and the hexagon pillars' side length was 5 μm. It was shown in Fig.2.3 and the parameters of these three geometric patterns were shown in Table 1. The pillar height d were 10 μm and 20 μm. It could be acquired by controlling the etching circles during the ICP etching.

Table 2.1. Characterization of Microstructure Geometric Parameters.

Shape of micro pillar	Area fraction *f*	K
Square	$\frac{a^2}{(a+b)^2}$	$\frac{a}{4}$
Triangle	$\frac{\sqrt{3}a^2}{(\sqrt{3}a+2b)^2}$	$\frac{\sqrt{3}}{12}a$
Hexagon	$\frac{3\sqrt{3}a^2}{2(\sqrt{3}a+b)(2a+b)}$	$\frac{\sqrt{3}}{4}a$

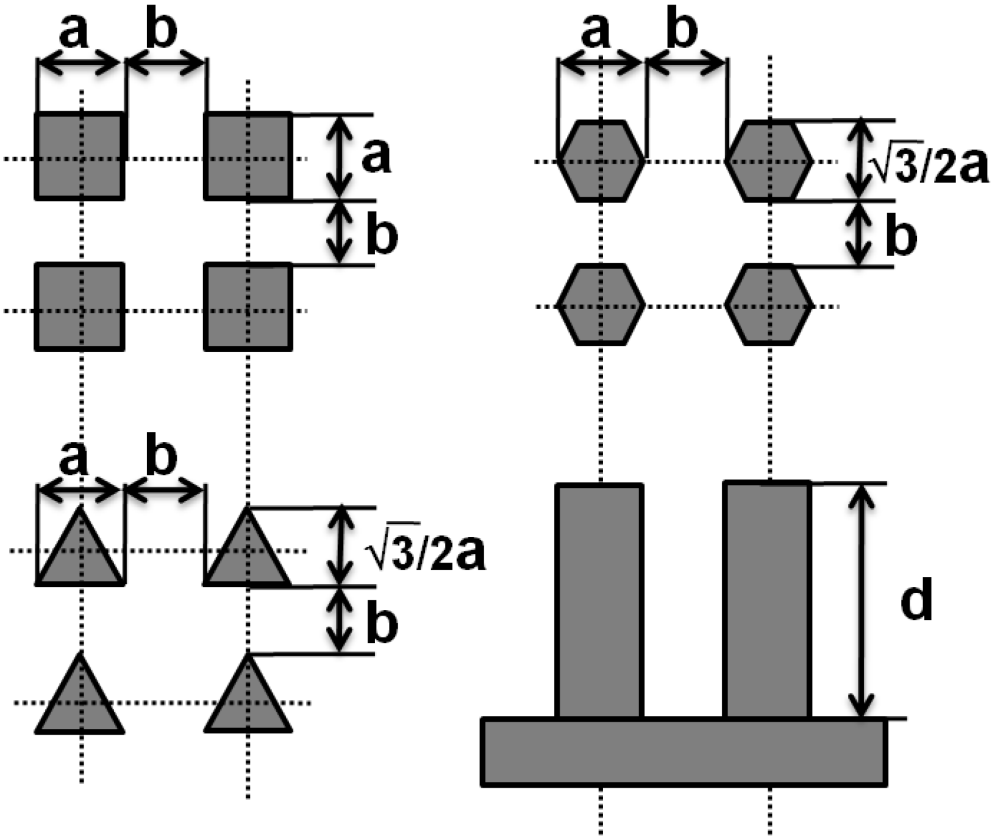

Fig.2.3. Microstructure distribution diagram

The fixed pillar heights (d = 10 μm and 20 μm) for all the pillar-structured surfaces was achieved by controlling the etching circles. The fabricated micro-structured surfaces were measured by the Confocal Laser Scanning Microscope (CLSM)，LEXTOLS4000, OLYMPUS. The fabricated micro-pillars' parameters and profiles were shown in Table 2.2, Table 2.3, and Fig.2.4. The fabricated microstructures have a small amount of manufacturing error in the mask error and fabrication process, but the error was within a reasonable error range.

Table 2.2. Actual measured parameters of microstructure with d = 10 µm

Sample	**Geometric designs**	**Side length a (µm) (10, 10, 5 µm)**	**Space b (µm) (10, 25, 50µm)**	**Depth d (µm) (10µm)**	**Area fraction *f***
SQU a10-b10-d10	Square1	10.120	9.986	10.882	0.2533
SQU a10-b25-d10	Square2	9.933	24.540	12.415	0.0838
SQU a10-b50-d10	Square3	9.867	49.333	14.694	0.0278
TRI a10-b10-d10	Triangle 4	10.373	10.373	12.656	0.1244
TRI a10-b25-d10	Triangle 5	9.867	25.299	11.147	0.0268
TRI a10-b50-d10	Triangle 6	9.614	50.345	11.868	0.0116
HEX a10-b10-d10	Hexagon 7	5.819	9.590	15.251	0.2107
HEX a10-b25-d10	Hexagon 8	5.819	25.046	12.715	0.0683
HEX a10-b50-d10	Hexagon 9	6.072	49.586	13.244	0.0258

Table 2.3. Actual measured parameters of microstructure with d = 20 µm

Sample	**Geometric Designs**	**Side Length a (µm) (10, 10, 5µm)**	**Space (µm) (10, 25, 50µm)**	**Depth (µm) (20 µm)**	**Area fraction f**
SQU a10-b10-d20	Square 1	10.879	9.361	20.226	0.2889
SQU a10-b25-d20	Square 2	10.879	24.540	19.325	0.0943
SQU a10-b50-d20	Square 3	10.626	49.333	20.288	0.0314
TRI a10-b10-d20	Triangle 4	9.843	9.867	19.138	0.1240
TRI a10-b25-d20	Triangle 5	10.095	25.238	18.165	0.0398
TRI a10-b50-d20	Triangle 6	9.590	50.233	18.799	0.0117
HEX a10-b10-d20	Hexagon 7	6.057	9.108	20.890	0.2376
HEX a10-b25-d20	Hexagon 8	7.067	24.287	19.294	0.0925
HEX a10-b50-d20	Hexagon 9	6.309	49.839	19.530	0.0255

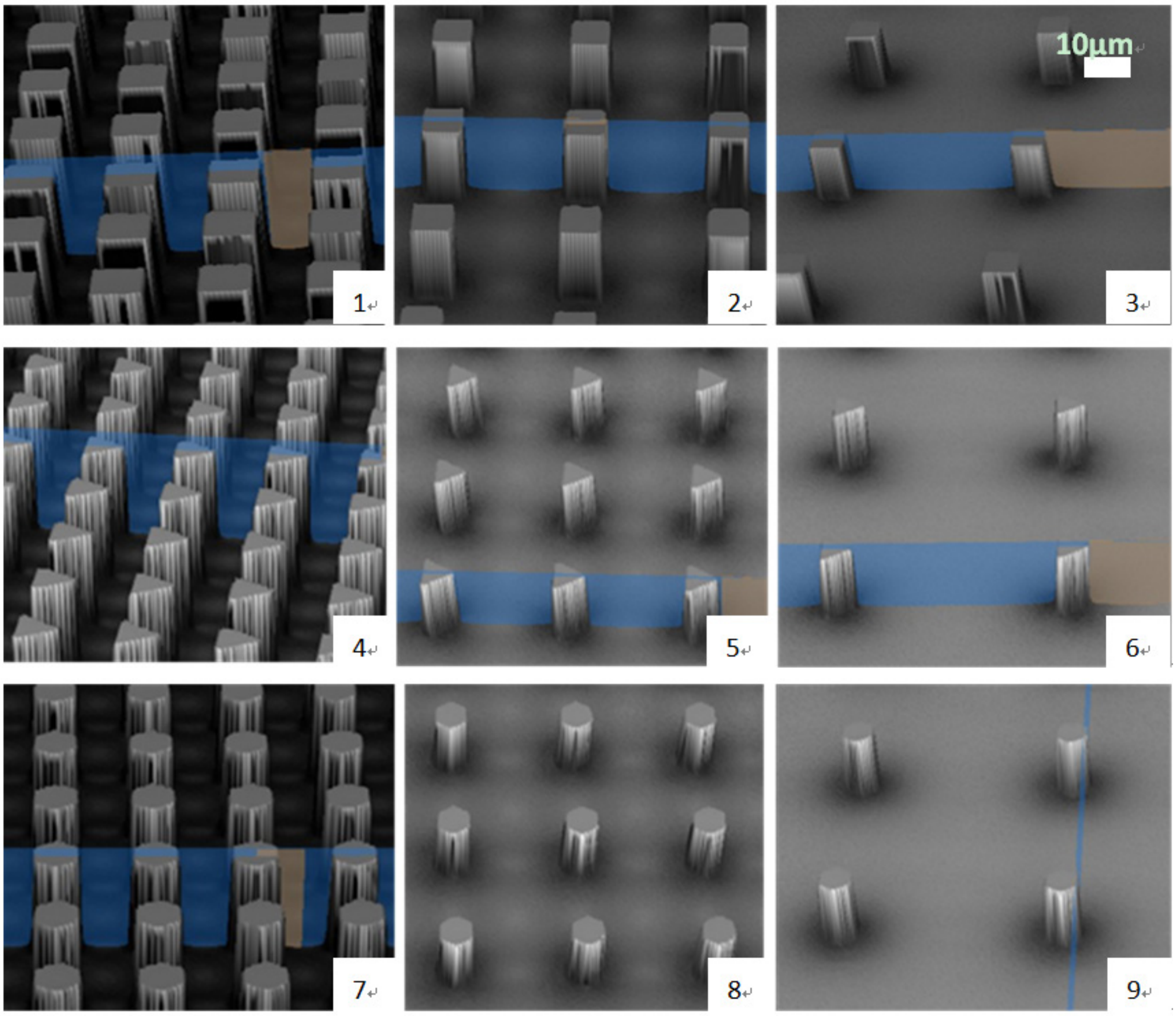

Fig.2.4. Three-dimensional images of micro-pillars with designed h = 20 µm, (1), (2), and (3) shown the a = 10 µm square micro-pillar structures with different space between the pillars, b = 10 µm, 25 µm, and 50 µm respectively. (4), (5), and (6) shows the a = 10µm triangle micro-pillar structures with different spaces between the pillars. b = 10 µm, 25 µm, and 50 µm respectively. (7), (8), and (9) shown the a = 10 µm hexagon micro-pillar structures (Side length = 5 µm) with different space between the pillars b = 10 µm, 25 µm, and 50 µm, respectively

As the roughness would influence the droplet contacting the surface of micro-pillar, it’s an important parameter on the micro-pillar top and were observed by the Confocal Laser Scanning Microscope (CLSM) and Atomic Force Microscope (AFM). The top surface on the micro-pillar had a root mean square roughness of 0.433 nm (5μm X 5μm) (as shown in the Fig.2.5) and was relatively smooth. It could be neglected in the contact angle test. Also, the surface roughness Ra of the bottom etched Si surface was approximately 0.2 μm.

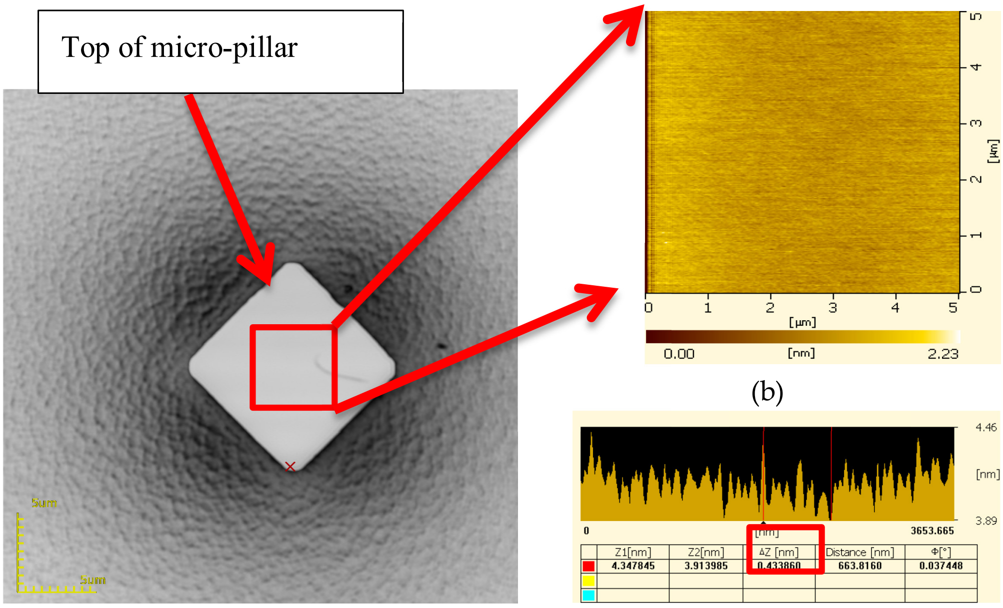

(a) (c)

Fig.2.5. Morphology of the micro-pillar top surface. (a) CLSM image of the square micro-pillar. (b), (c) AFM images of the typical topography of the micro-pillar top surface (5μm X 5μm). The root mean square roughness is 0.433nm.

2.3.2. Contact Angle Measurement

The relationship of vapor, liquid and solid of droplet could be described in single-phase regime. Contact angle measurements could be used to describe the temperature-dependent wettability of single-phase regime droplets. During the contact angle (CA) measurement the KRUSS temperature controlled chamber TC21 was used to control the temperature. The Droplet Sharp Analyzer DSA25 was used to place a 10-μL-water droplet on the micro-structured substrate. (volume for a drop to not be affected by gravity)

During the measuring, a range of contact angles would be obtained. At the advancing edge of a liquid drop, the upper limit of the range was obtained which is the advancing contact angle θ_A. At the receding edge, the lower limit of the range was obtained which is the receding contact angle θ_R.

In the research, the used DI water (18.2 MΩ•cm) was purified in a DI water system. The fabricated Si wafer was cleared by the RCA cleaning process before taking the contact angle measurement. The static advancing and receding contact angles were measured three times by using the polynomial fitting method on each surface. The advancing and receding angles were measured by slowly pumping liquid into or out of a droplet. The used DI water (18.2 MΩ•cm) was purified in a DI water system. The fabricated Si wafer was cleared by the RCA cleaning process before taking the contact angle measurement.

2.4. Results and Discussion

There were lots of contact angles (CA) during the measurement on the micro-structured surface. But a drop should have a stable point at the energetically lowest point. It was named equilibrium CA.

During the research, all the droplets were Cassie-Baxter state on the micro-structured surfaces but the droplet on the square-pillar surface with pillar space b=50 μm and pillar height d=10 μm were at 50 °C.

The measurement result data of the advancing and receding contact angles could be used to calculate the equilibrium CA by using the Tadmor equation [68]. The hysteresis was determined by some dimensionless parameter which was normalized line energy.

$$\theta = \arccos\left(\frac{\tau_A cos\theta_A + \tau_R cos\theta_R}{\tau_A + \tau_R}\right) \tag{2.4}$$

where $\tau_A \equiv \left(\frac{sin^3\theta_A}{(2-3cos\theta_A+cos^3\theta_A)}\right)^{1/3}$

and $\tau_R \equiv \left(\frac{sin^3\theta_R}{(2-3cos\theta_R+cos^3\theta_R)}\right)^{1/3}$

2.4.1. Profile Characterization and Temperature Effect on Contact Angle

From the measuring data, the CAs were lager on the micro-structured surfaces than the smooth surface as the roughness enhances the wetting. The profile characterization effects on the micro-surface were shown in the Fig.2.6.

The contact angles on the micro-structured surface with different temperatures (30 °C to 90 °C) were shown in Fig.2.6. From the Figures, several effects could be concluded as following:

The CAs and area fraction f decreased when the space between the pillars became wider.

The pillar height’s increasing leads to the equilibrium CA increases.

With the pillar height increases the equilibrium CA increases.

The CAs decreases when temperature increases with pillar height 20 μm.

From the Fig.2.6(a) and (b), for the hexagon micro-pillars, the CAs with the higher micro-pillars were more lineally with temperature increasing.

The air layer in the micro-pillars buffered the temperature effect. With square and triangle micro-pillars, the similar results were shown on the square and triangle micro-pillar surface.

With the 10 μm pillar height and the CA curve of the micro-pillar surface with space b 10 μm, it rose first and then went down when the sample was heated. The same result as the CA curves of the hexagon- and triangle-pillar surfaces with space b were 20 μm.

But CA curves of the surface with square-pillars showed the opposite way. It went down first and then rose.

With the space b was 50 μm, the CA curve of these micro-pillar surfaces showed the lineal change as the temperature increased. This phenomenon caused by heated air layer in the micro-pillars and the temperature affected surface tension coefficients

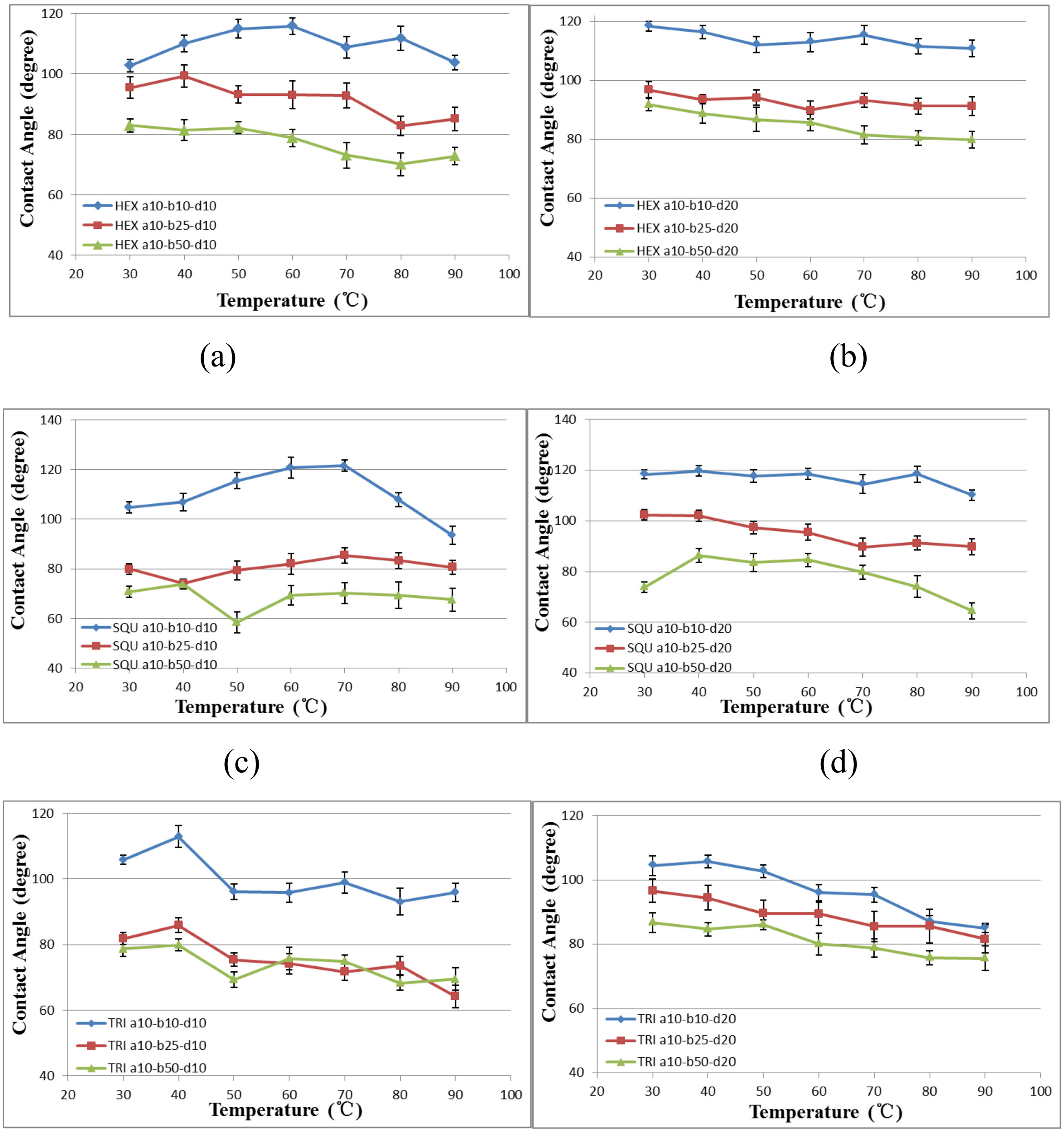

(a) (b)

(c) (d)

(e) (f)

Fig.2.6. Contact angle curve of the same shape's micro-structured surface at different temperatures. (a) and (b) show the contact angles at different temperatures on the hexagon micro-pillar surfaces with d = 10 μm and 20 μm respectively. (c) and (d) shows the contact angles at different temperatures on the square micro-pillar surfaces with d = 10 μm and 20 μm respectively. (e) and (f) shows the contact angles at different temperatures on the triangle micro-pillar surfaces with d = 10 μm and 20 μm, respectively.

2.4.2. Shape and Temperature Effect on Contact Angle

From the Fig.2.7, several effect could be concluded as following:

On these three shapes the CAs were first increased and then decreased.As the obtuse angle may avoid the stress concentration on the solid-liquid contact line, the Hexagon-pillar and Square-pillar micro-structured surfaces showed the higher CA when the parameters were the same.

With the temperatures went higher, the micro-pillar structured surfaces with the space between the pillars b = 10 μm decreased.

This phenomenon reduces rapidly when the space between the pillars increases, but this was nearly invisible in the CA measurements on the micro-structured surface with a pillar depth of d = 20 μm.

From Fig.2.7 (c) and (e), it was shown that the Hexagon-pillar surface has higher CA than the other two type micro-structured surfaces with space between the pillars b = 25 μm and 50 μm and pillar depth was 10 μm. when pillar depth was 20 μm, the CA on Square-pillar surface with pace between the pillars b = 10 μm and 25 μm was higher (see Fig.2.7 (b), (d)).

With the space between the pillars b = 10 μm and pillar depth d = 10 μm, the CA on triangle-pillar surface went down when the temperature rose over 40 °C. On the Square- and Hexagon-pillar surface, the CA went down from 70 °C and 60 °C respectively (Fig. 2.7(a)).

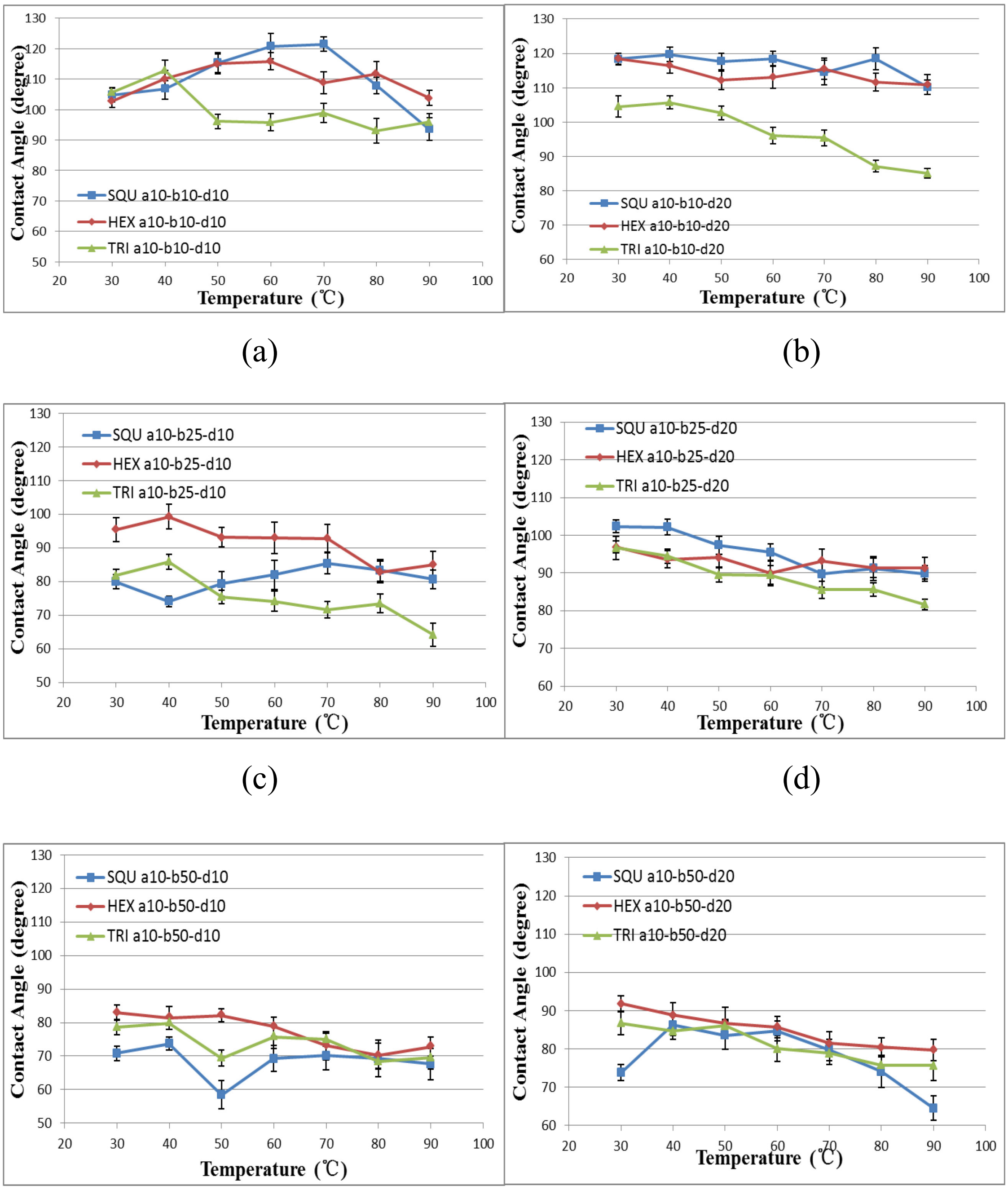

(a) (b)

(c) (d)

(e) (f)

Fig.2.7. Contact angle curve of the same designed parameter's micro-structured surface at different temperatures. (a), (c), and (e) show the contact angles at different temperatures on the three shapes with micro-pillar surfaces with space b = 10 µm, 25 µm, and 50 µm respectively when the depth d = 10 µm. (b), (d), and (f) show the contact angles at different temperatures on the three shapes with micro-pillar surfaces and space b = 10 µm, 25 µm and 50 µm respectively when the depth d = 20 µm.

2.5. Conclusions

In this research three shapes of micro-pillar surfaces were designed with different space and height. They were successfully fabricated by using photolithography and ICP etching techniques. 10 μL DI water droplet was used to be observed the wetting behavior on the fabricated surfaces. The wetting behavior of surfaces with different micro-structures from 30 °C to 90 °C was described in this paper. From the measurement result, all the droplets were Cassie-Baxter state on the micro-structured surfaces except the droplet on the sample SQU a10-b50-d10 at 50 °C. There were several conclusions from the observation and the primary conclusions are as follows:

The contact angles increased when the pillar height increased.

With the wider pillar-structure space the contact angle decreased.

With the pillar height 10 μm, the CAs were first increased and then decreased when the temperature rose.

The relationship of temperature and CAs on the micro-structured surfaces with pillar height d=20 μm was nearly linearly dependent.

On all the three-phase contact line, the contact angles were fluctuated by both the temperature change and the microstructure effect.

Chapter 3

High Temperature Wetting Transition on Microstructured Superhydrophobic Surface

Abstract:

Superhydrophobic surface has attracted significant attention since their potentiality to industrial and academic applications. Moreover, superhydrophobic surface wettability at non-ambient temperature, especially at high temperature (but not boiling) was of great importance in many industrial processes. In this paper, we designed and fabricated 4 series superhydrophobic micro-pillar surfaces on the Silicon wafers to investigate wettability at different temperatures. These micro-pillar surfaces were fabricated by photolithography and ICP etching technologies. The temperature-dependent wettability of DI water droplets was characterized using contact angle measurements. The wetting behavior was observed to be different on the surfaces, and the wetting transition occurred at a specific temperature.

3.1. Introduction

Inspired by the natural phenomena such as self-cleaning property on lotus leaves and fish scale [5, 11, 48], directional adhesion on butterfly wings [49], water striders walking on the water surface [6] antifogging of mosquito eyes [50], Wetting of superhydrophobic surfaces has received significant attention from both academic and industry due to their spectacular advantage and wide application such as self-cleaning materials[16], water collecting means[9], friction drag reduction surfaces[69],oil\water separation[70], and droplet control in microfluidic device [71]. The superhydrophobic surface with contact angle (CA) > 150°and sliding angle (SA) below 10° was recognized as “lotus effect”, on which the droplets maintain a spherical shape and roll off easily.

Various methods had been developed to generate the superhydrophobic surfaces on glass, semiconductors, polymers and metals by using physical and chemical treatment.

Since Wenzel and Cassie reported the effect of roughness on surface wettability [42, 43], research found the way to enhance the wetting by modifying the surface roughness. Researchers created varies methods to fabricate the hierarchical structures such as lithography[72], electro deposition[22], chemical deposition[23], sputtering[24], anodization[25], and ultrafast laser surface texturing[73]. Superhydrophobic surface, typically an effect enhanced by surface roughness on hydrophobic surfaces, has recently attracted great attention because of the easy fabrication of microstructured surfaces with superhydrophobicity.

Droplets on chemically or microstructured surfaces can generally adopt two different states[54]: the Wenzel state, in which the liquid completely wets the entire surface (see Fig.3.1(a)), or the Cassie-Baxter state, in which the droplet only partly wets the surface, leaving air in between the microstructures under the droplet (see Fig.3.1(b)).

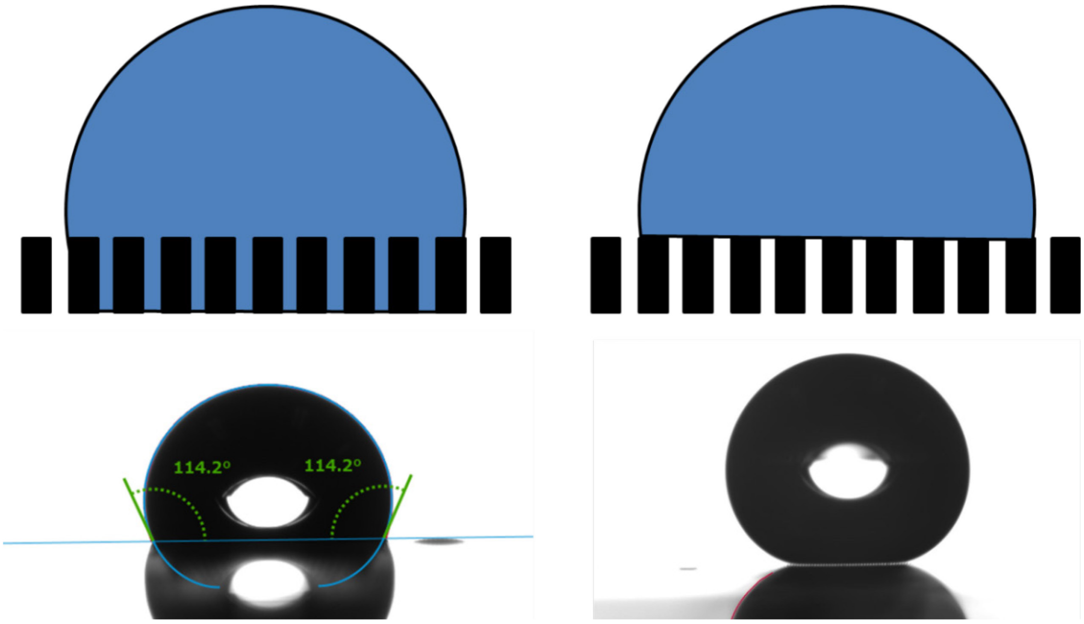

(a) Wenzel state **(b)**Cassie-Baxter state

Fig.3.1. States of droplets

Moreover, surface wettability at high temperature (30 to 90℃), is importance in industrial processes[55], such as water transportation and metal processing [38]. Recently, several advances have been made, like the superhydrophobic surfaces hot water repellent [56], the wetting-controllable thermally responsive materials fabrication [58, 59], wetting transition on hydrophobic microstructures surface during evaporation[60], low temperature heat exchanging on hydrophobic surfaces[63]. The theory and applications of droplet wetting behavior on a hot surface is very important in the solid–liquid heat transfer system[64].

However, the effect of surface morphology and temperature effect on the wetting behavior at high temperature as not been studied systematically. The investigation of the wetting behavior of surfaces with different micro-structures from 30 to 90℃ was described in this paper.

The goal of the present study was to investigate the effects of surface microstructure and temperature on the superhydrophobic surfaces. Four shapes micro-pillars with deferent distributed parameters microstructured surfaces with different wettability Silicon wafer were fabricated to investigate wettability at different temperatures. Wafers with micro-pillars arrays were obtained by photolithography and ICP etching.

3.2. Theory and calculation

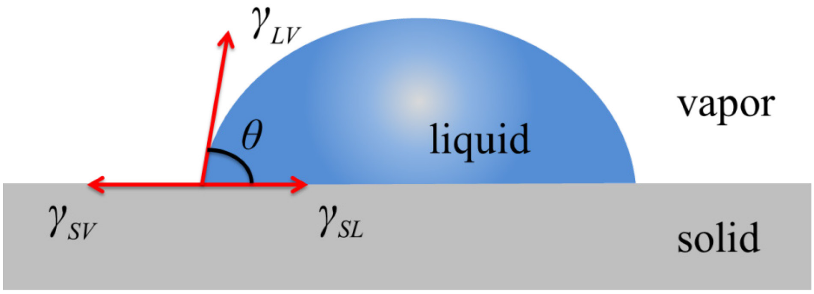

Fig.3.2. Illustration of the contact angle

The contact angle of a water droplet on a smooth and chemical homogeneous surface (as shown in Fig.3.2) can be computed by the Young's equation [15].

$$\cos\theta = \frac{\gamma_{SV}-\gamma_{SL}}{\gamma_{LV}} \tag{3.1}$$

where γ_{SV}, γ_{SL} and$\gamma_{LV,}$ are the surface tension coefficients on solid-vapor, solid-liquid, and liquid-vapor interfaces, respectively.

Both the Wenzel and Cassie-Baxter state has the following relation with the intrinsic contact angle θ and the topography of the roughness structure. Wenzel's theory described the non-composite state where water penetrates into the gap space when a droplet on a rough surface [12].

$$\cos\theta w= r\cos\theta \tag{3.2}$$

Cassie's theory related to the composite state where the droplet on a rough surface traps air between solid and liquid. The wetting characteristic of such a surface was first addressed by Cassie and Baxter [13] and the apparent contact angle θc was predicted by the following equation.

$$\cos\theta c= (\gamma^*_{SV} - \gamma^*_{SL}) / \gamma_{LV} \tag{3.3}$$

where $\gamma^*_{SV} = f\gamma_{SV}$ and $\gamma^*_{SL} = (1-f)\gamma_{LV} + f\gamma_{SL}$, f is the area fraction. Researchers considered the three-phase contact line tension on the liquid-vapor-solid phase boundary and presented a new model to predict the contact angle of a water droplet on a rough surface.

$$\cos\theta c^*=-1+(1+\cos\theta)(1 - -\lambda/(K(1+\cos\theta)\gamma_{LV}))f \tag{3.4}$$

It was clear that the surface roughness can greatly influence the behavior of water drop on solid surface. On one hand, rough-ness increases the surface area of the solid, which geometrically enhances hydrophobicity (Wenzel state). On the other hand, vapor can remain trapped below the drop, which also leads to a superhydrophobic behavior, because the drop sits partially on vapor (Cassie- Baxter state).

3.3 Experimental Method

3.3.1 Microstructures Surface Design and Fabrication

Silicon wafer with various structures were fabricated to investigate wettability at different temperatures. 5-μm-level micro-pillars were uniformly distributed in a designated section with different space between the pillars.

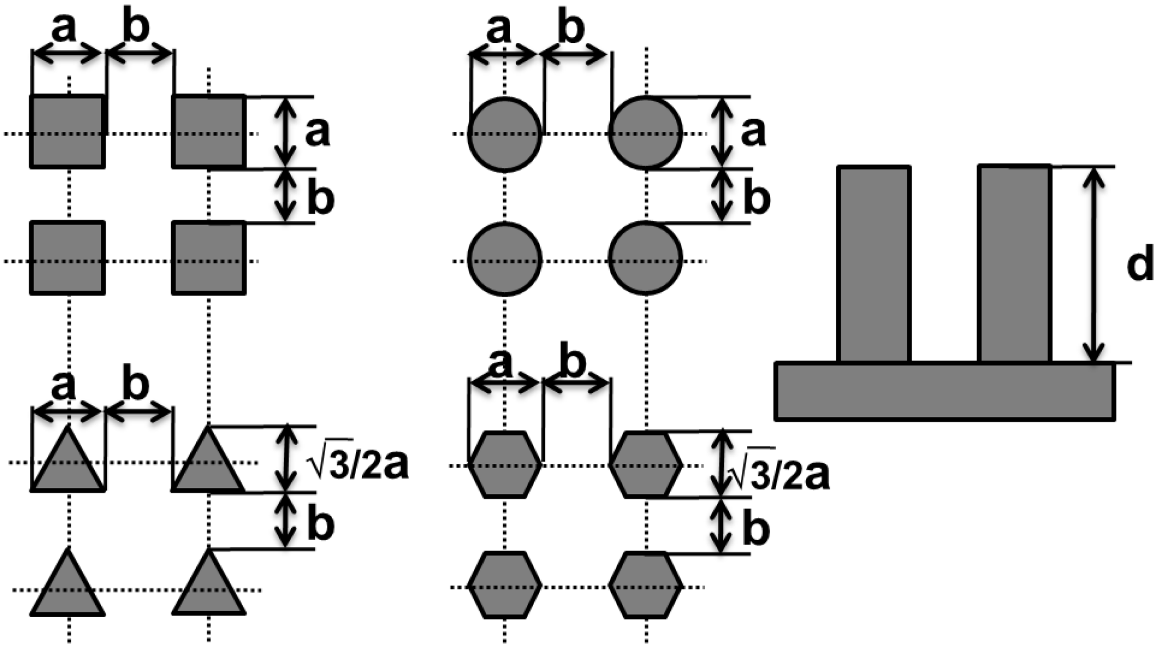

Fig.3.3. Microstructure distribution diagram

The micro-structured surfaces were fabricated employed the photolithography and Inductively Coupled Plasma (ICP) etching techniques. The side lengths or diameter of these micro-pillars a = 5 μm(for Triangle-, Square-, and Circle-pillars) and the diagonal of hexagon-pillars a= 5 μm (side length a= 2.5μm for Hexagon-pillars), as shown in Fig.3.3. These four-type pillars are uniformly distributed in a rectangular grid with four different spaces between the pillars for each shape pillar. The values of the space b= 5, 12.5, 25 and 50 μm. Two fixed pillar height (etching depth) d = 5 and 10 μm was achieved by controlling the etching parameter and time.

These micro-pillars were uniformly distributed in a square grid on a glass mask. Before the fabricating process, a 400 μm thick 4 inch Silicon wafer ((100), p-type) was cleaned in RCA process rinsed by the DI water and dry, then a 1μm positive photoresist layer (s1805) was spinning-coated on the Si surface. In the next step, the required pattern was transferred from the mask to the photoresist layer by UV exposing; subsequently the photoresist was partly removed by the developer. The uncovered Si was etched in the ICP etcher (STS MC21) to finally fabricate the roughness pattern on the Si wafer.

3.3.2 Surface Characterization

Before the contact angle testing, the surface was cleaned in a RCA process again, then rinsed with DI water and dried. The fabricated micro-pillars' parameters and profiles were shown in the table 3.1 and 3. 2.

Table 3.1. Actual measured parameters of microstructure with d = 5 μm

Sample	**shape**	**a(5μm)**	**b**	**d(5μm)**	**f**
TRI-a5-b5-d5	Triangle	4.402	5.229	7.562	0.096359332
TRI-a5-b12.5-d5	Triangle	4.429	13.185	5.606	0.028331436
TRI-a5-b25-d5	Triangle	4.36	26.829	7.449	0.008623239
TRI-a5-b50-h5	Triangle	4.692	51.297	6.517	0.00307541
SQU- a5-b5-d5	Square	4.772	5.24	6.788	0.224677142
SQU- a5-b12.5-d5	Square	4.879	13.673	5.805	0.06916401
SQU- a5-b25-d5	Square	4.717	25.205	6.389	0.02485138
SQU- a5-b50-d5	Square	4.542	52.453	7.079	0.006350688
HEX- a5-b5-d5	Hexagon	4.702	6.235	6.818	0.127384557
HEX- a5-b12.5-d5	Hexagon	4.879	13.673	6.545	0.046562936
HEX- a5-b25-d5	Hexagon	4.542	25.648	6.629	0.015003479
HEX- a5-b50-d5	Hexagon	4.373	51.947	6.875	0.0039569
CIR- a5-b5-d5	Circle	4.921	5.299	6.994	0.182088287
CIR- a5-b12.5-d5	Circle	4.431	13.673	6.754	0.047046952
CIR- a5-b25-d5	Circle	4.748	26.311	6.762	0.018353697
CIR- a5-b50-d5	Circle	4.385	50.598	7.116	0.004995275

Table 3.2. Actual measured parameters of microstructure with d = 10 μm

Sample	**shape**	**a(5μm)**	**b**	**d(10μm)**	**f**
TRI-a5-b5-d10	Triangle	4.238	5.831	12.261	0.081292261
TRI-a5-b12.5-d10	Triangle	4.438	13.673	12.610	0.026882985
TRI-a5-b25-d10	Triangle	4.342	26.323	12.659	0.008849137
TRI-a5-b50-h10	Triangle	4.338	51.616	12.182	0.002629905
SQU- a5-b5-d10	Square	4.811	5.271	11.456	0.227707496
SQU- a5-b12.5-d10	Square	5.819	13.155	11.587	0.094054358
SQU- a5-b25-d10	Square	5.060	26.311	11.238	0.026016227
SQU- a5-b50-d10	Square	5.013	51.357	12.211	0.007908595
HEX- a5-b5-d10	Hexagon	4.611	5.687	11.698	0.138527342
HEX- a5-b12.5-d10	Hexagon	4.545	13.086	11.401	0.044705418
HEX- a5-b25-d10	Hexagon	4.411	26.000	10.913	0.01393529
HEX- a5-b50-d10	Hexagon	4.292	51.781	11.648	0.003844753
CIR- a5-b5-d10	Circle	4.813	5.831	11.760	0.160582814
CIR- a5-b12.5-10	Circle	4.807	12.903	11.883	0.057861301
CIR- a5-b25-d10	Circle	4.607	25.552	10.941	0.018326504
CIR- a5-b50-d10	Circle	4.554	50.851	11.929	0.005305975

3.3.3 Contact Angle Measurements

Contact angle (CA) measurements were realized at different temperatures with the KRUSS temperature controlled chamber TC21 for temperature control of samples and Droplet Sharp Analyzer DSA25 for contact angle measurement. The 10 μL DI water droplets were produced by the automatic controlled syringe. This automatic syringe was used to generate droplets with an injection rate of 0.15mL/min to reduce the inertial effects. All the static CAs were measured three times using the polynomial fitting method on each surface.

3.4 Results and Discussion

3.4.1 Profile and Temperature Effect on Contact Angle

The wetting behavior of these fabricated surfaces at various temperatures was investigated. The static contact angles were measured three times on each type surface. The results were shown in the following Figures. The error bars were undetectable in some figures since the deviation was less than 3° .

Fig.3.4 (a) and (b) showed the contact angles (CAs) on Circle-pillar surfaces with different area fraction *f* at various temperatures. The superhydrophobic wettability was observed on the Circle-pillar surfaces with pillar height d=5 and 10μm at the room temperature except the surface named Cir a5-b50-d10. Then these surfaces were heated using a temperature controlled chamber, when the pillar height was 5μm, the CA transition on the surfaces named Cir a5-b5-d5 and Cir a5-b12.5-d5 was almost indiscernible, the CAs on surface named Cir a5-b25-d5 had an almost insensible change when the surface temperature was below 60℃, but the wettability on this surface transited from superhydrophobic to hydrophilic when the temperature was over 60℃, the CAs was less the untreated Si surface. The CAs on the surface named Cir a5-b50-d5 decreased fast with the temperature increased, the surface wettability transited from superhydrophobic to hydrophilic when the temperature was over 30℃ , the CAs on this surface even less than the untreated Si surface when the surface temperature was over 60℃.

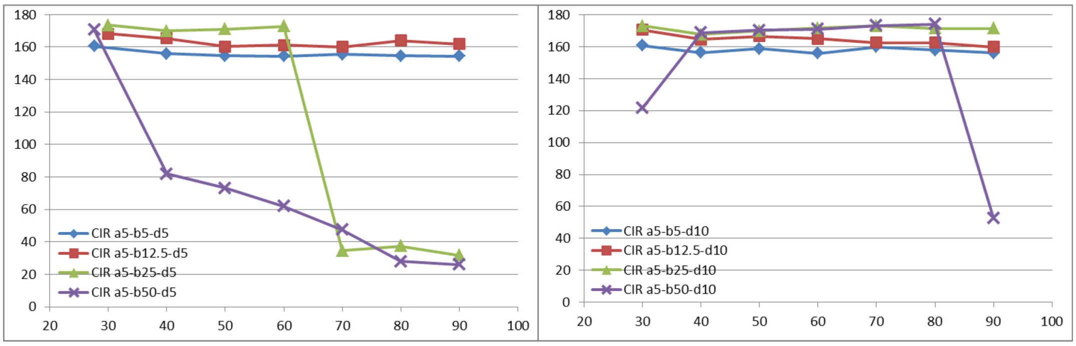

(a) pillar height d=5μm (b) pillar height d=10μm

Fig.3.4 Contact angles on circle-pillar surfaces

When the pillar height was 10 μm, the CAs were increased with the space between pillars b increased and had an insignificant change for each surface with the temperature increased. But the CA of Cir a5-b50-d10 surface was around 121°at room temperature that was less than other surface. However, the CA on this surface was increased fast when the temperature was increased to 40℃, and then kept almost constant until 80℃, when the surface was heated over 80℃, the wetting transited from superhydrophobic to hydrophilic.

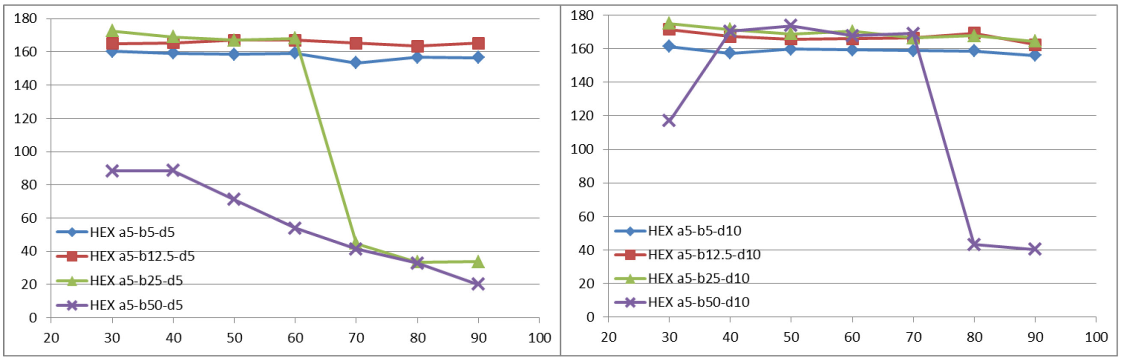

(a) pillar height d=5μm (b) pillar height d=10μm

Fig.3.5 Contact angles on hexagon-pillar surfaces

Fig.3.5 (a) and (b) showed the contact angles on hexagon-pillar surfaces with different area fraction *f* at various temperatures. The wettability on the hexagon-pillar surfaces was similar to wetting behaviors the circle-pillar surface. When the pillar height d=5 μm, the surfaces shown the superhydrophobic wettability except the surface with space between pillar b= 50 μm at room temperature. The CAs had small fluctuations on the surface with space between pillar b= 5 and 12.5 μm during temperature increasing. However, the surface with space between pillar b= 25 μm lost superhydrophobic wettability and transited to hydrophilic when the temperature was over 60℃,the stage of droplet on the surface was transited from Cassie-Baxter stage to Wenzel stage (as shown in Fig.3.5). Surface with space between pillar b=50 μm shown hydrophilic wettability, and the CAs decreased with temperature increased.

When the pillar height d=10 μm, the result was similar to the circle-pillar surface with same parameters, The CAs had an insignificant change on the heated surface with space between pillar b=5, 12.5, 25 μm, these 3 types surfaces kept the superhydrophobic wettability invariable and the CAs were more than 150° . The wetting behaviors of droplet on the surface with space between pillar b=50 μm transited from hydrophobic to superhydrophobic and finally changed to hydrophilic during temperature increasing.

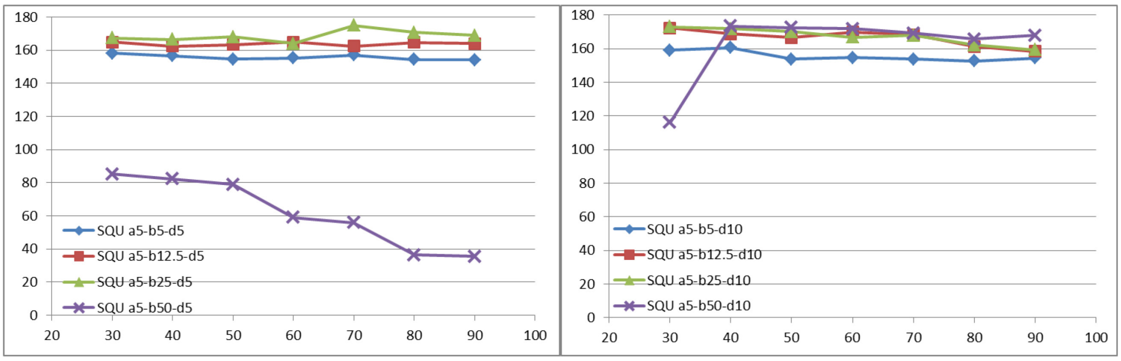

(a) pillar height d=5μm (b) pillar height d=10μm

Fig.3.6 Contact angles on square-pillar surfaces

Fig.3.6 (a) and (b) showed the contact angles on square-pillar surfaces with different area fraction *f* at various temperatures. When the pillar height d= 5 μm, the CAs on the surface with space between pillars b= 5, 12.5, 25 had small fluctuations with the temperature increased. However, the surface with space between pillars b= 50 μm was shown hydrophilic wettability; The CAs on this surface was decreased with the temperature increased and less than 40 ∘ at temperature was over 80 ℃, more hydrophilic than the smooth Si surface.

When the pillar height d=10 μm, all 4 types square-pillar surfaces had superhydrophobic wettability but the surface with space between pillar b=50 μm at room temperature (30 ℃). However, the CA on the surface named SQU a5-b50-d10 increased very fast when the surface temperature risen to 40 ℃, therefrom, these 4 types square-pillar surface kept the superhydrophobic wettability invariable with the temperature increased.

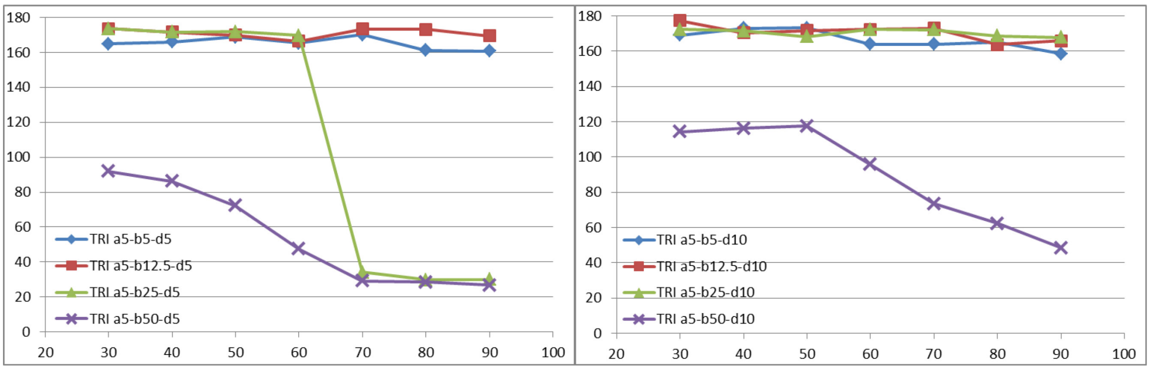

(a) pillar height d=5μm (b) pillar height d=10μm

Fig.3.7 Contact angles on triangle-pillar surfaces

Fig.3.7 (a) and (b) showed the contact angles on square-pillar surfaces with different area fraction *f* at various temperatures. When the triangle-pillar height d=5μm, the CAs had slight fluctuation for the surfaces with space between pillars b=5 and 12.5 μm. The droplet stage on the surface with space between pillars b=25 μm was transited from superhydrophobic to hydrophilic when the surface temperature raised from 60 to 70℃, the wettability of this surface was stable each stage when the surface temperature below 60 ℃ and over 70 ℃. The CA on the surface with space between pillars b=50 μm decreased with the temperature increased, and the wettability on this surface was hydrophilic (as shown in Fig.3.7 (a)).

When the pillar height d=10 μm, the surfaces shown the stable superhydrophobic wettability except the surface with space between pillars b=50 μm. The CAs on these superhydrophobic surfaces had just small wiggles with the temperature increased. The CAs was first increased slowly and then decrease fast on the surface with space between pillars b=50 μm, the hydrophobic surface transited to hydrophilic surface with the temperature increased (as shown in Fig.3.7 (b)).

3.4.2 Shape and Temperature Effect on Contact Angle

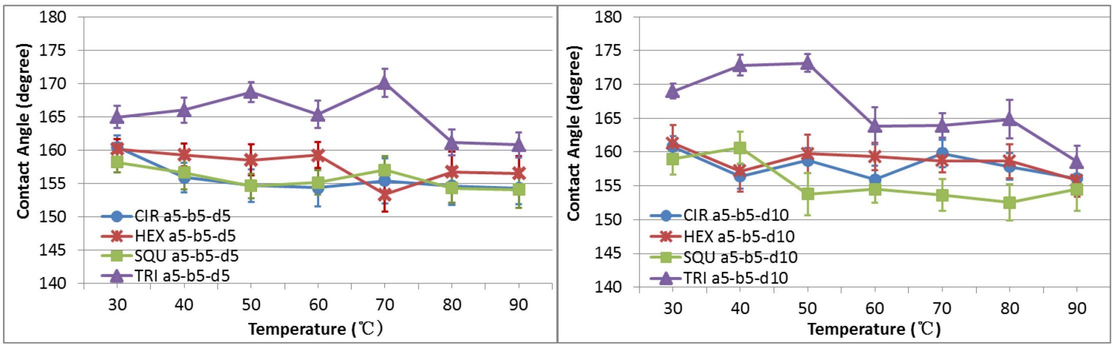

(a) pillar height d=5μm (b) pillar height d=10μm

Fig.3.8 Contact angles on micro-pillar surfaces with b=5μm

Fig.3.8 (a) and (b) indicated effect of pillar shape and surface temperature on the CA for constant space b=5 μm and height d=5 and 10μm. The four shape surfaces with pillar side length a=5μm and space between pillars b= 5μm shown superhydrophobic wettability for both 5 and 10 μm high pillars. All the CAs in Fig.3.8 were over 150◦, moreover, the value of CAs on the triangle-pillar surface were obviously higher than other 3 shapes. However, when the pillar height d=5 μm, the CAs were decreased approximately linearly with temperature increased on the other 3 shape surface except the triangle one. The CA on triangle-pillar surface were increased first and then decreased with temperature increased. When the pillar height d=10 μm, the droplet wetting behaviors on four shape surfaces shown similar variation, but the fluctuation of CAs were significant.

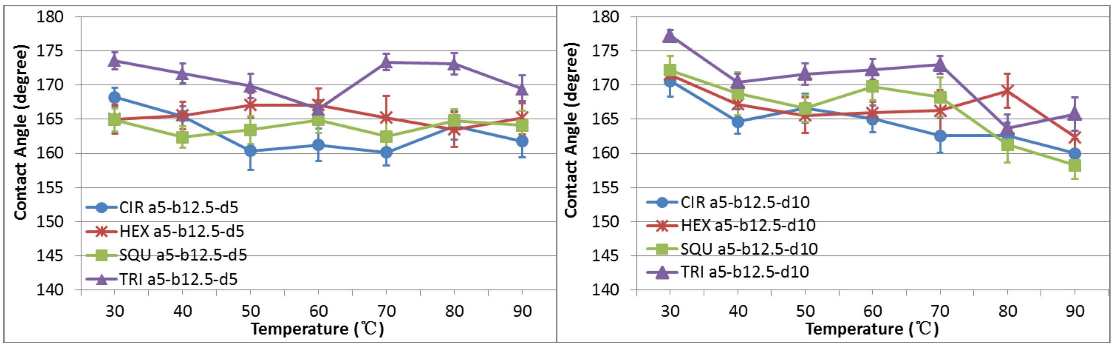

(a) pillar height d=5μm (b) pillar height d=10μm

Fig.3.9 Contact angles on micro-pillar surfaces with b=12.5μm

Fig.3.9 (a) and (b) indicated effect of pillar shape and surface temperature on the CA for constant space b=12.5 μm and height d=5 and 10μm. The CAs on the triangle-pillar surface were large than other three shapes but the difference was little. When pillar height d=5μm, the CAs on circle-, hexagon-, and square-pillar surface were fluctuated up and down between 160◦ to 170◦, but not decreased obviously with temperature increased. When pillar height d=10 μm, The CAs on the four shape surface were decreased with temperature increased, however, the change curve of CAs had a Wave protruding in the surfaces heated process.

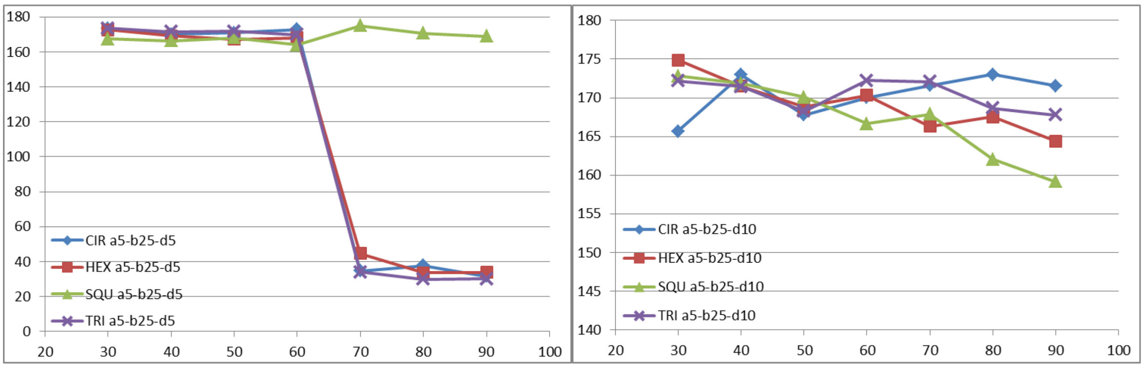

(a) pillar height d=5μm (b) pillar height d=10μm

Fig.3.10 Contact angles on micro-pillar surfaces with b=25μm

Fig.3.10 (a) and (b) indicated the CA variation of the four shape surfaces with the space between pillars b=25μm. When the pillar height d=5μm, the wettability on the circle-, hexagon-, and triangle-pillar surfaces had obviously transitions from superhydrophobic to hydrophilic between 60 and 70℃. However, the square-pillar surface still kept the superhydrophobic wettability with temperature increased. When the pillar height d=10 μm, all the four shape surfaces had the superhydrophobic wettability. The CAs on the hexagon- and square-pillars surfaces were decrease with temperature increased. However, the CAs on circle- and triangle-pillars surfaces were fluctuated up and down between 165∘ to 175∘.

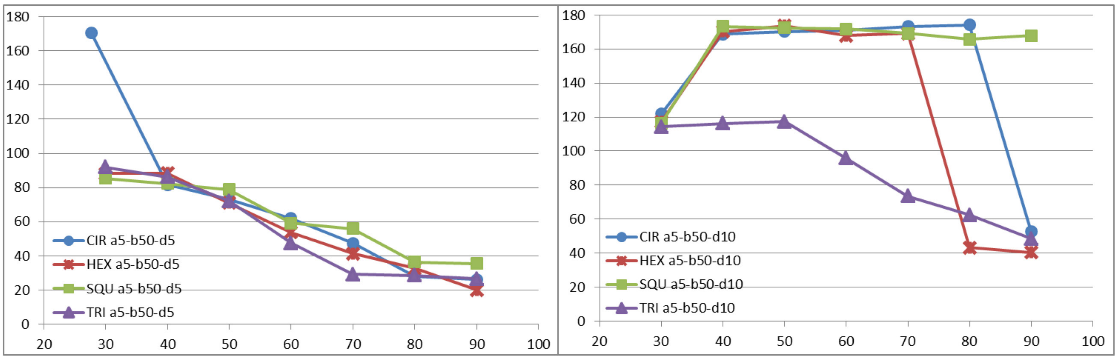

(a) pillar height d=5μm (b) pillar height d=10μm

Fig.3.11 Contact angles on micro-pillar surfaces with b=50μm

Fig.3.11 (a) and (b) indicated the CA change curve of the four shape surfaces with the space between pillars b=50 μm. When pillar height d=5μm, only circle-pillar surface had superhydrophobic wettability at 30 ℃, CAs of other three shape surfaces was around 90 °. All CAs were decreased with temperature increased on four shape surfaces. When pillar height d=10 μm, the CAs on the four shape surfaces were around 115◦ at 30 ℃. However, the CAs on the circle-, hexagon-, and square-pillar surfaces increased fast with the temperature increased to 40 ℃, the surfaces shown superhydrophobic wettability when the surfaces temperature was over 40 ℃, the square-pillar surface kept the superhydrophobic wettability with the temperature increased to 90 ℃. However, the wettability of hexagon- and circle-pillar surfaces transited from superhydrophobic to hydrophilic at 80 and 90 ℃ respectively. The CAs on the triangle-pillar surface increased insignificantly first and then decreased with temperature increased.

3.4.3 Droplet Stage Transition

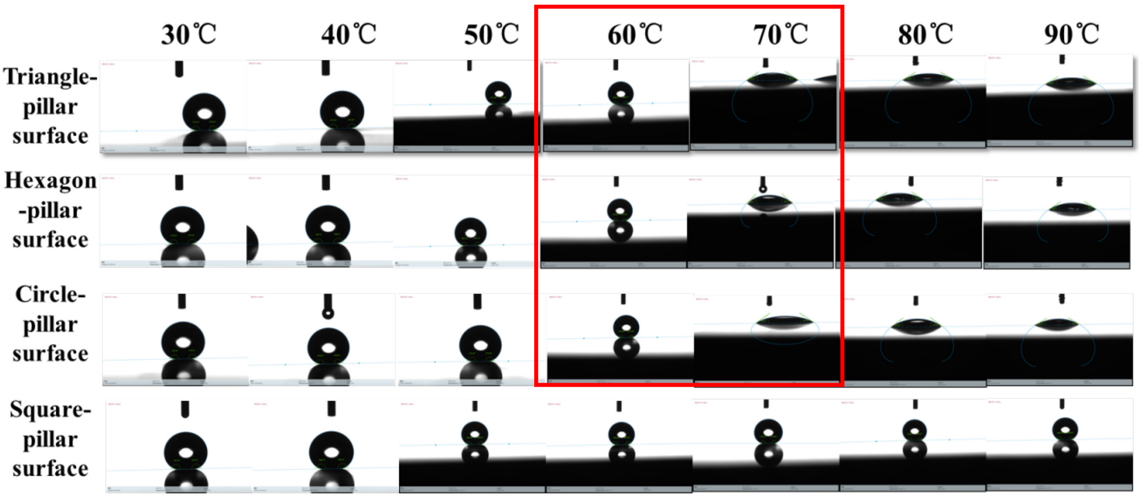

Fig.3.12. Water droplet on the micro-pillar surfaces with b= 25 μm and d=5 μm

As stated in the introduction, the droplet state on a roundness surface had Wenzel and Cassie-Baxter state. Under certain external stimuli, such as pressure, vibration or temperature, the Cassie-Baxter wetting state could be converted into the Wenzel state. In this research, when the space between pillars b=25 μm, and pillar height d= 5μm, the droplet sited on the 4 shapes micro-pillar surfaces in a Cassie-Baxter state at room temperature. During the heating process, the wetting state on triangle- hexagon- and circle-pillar were transited from Cassie-Baxter state to Wenzel state, when the surface temperature was over 60 ℃ (see Fig.3.12).

These wetting state transitions could be attributed to the temperature effect on the surface tension. The water droplet on the space between the pillars may be held by the Laplace pressure (P_L) and the Vapor pressure (P_V) to stand up to the gravity(mg) (as shown in Fig.3.13) .Here, the

Laplace pressure could be given as

$$P_L = 2\,\gamma_{LV} / R \qquad (3.5)$$

When surface temperature increasing, surface tension γ_{LV} may decrease. Therefore, Laplace pressure was decreased.

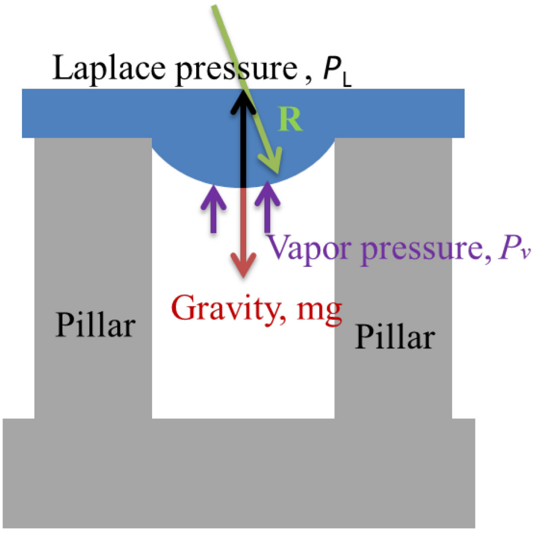

Fig.3.13 . Schematic illustration of water droplet on micro-pillars surface

The vapor pressure was a function of the vapor volume and temperature. If the Laplace pressure and the Vapor pressure can not stand up to the gravity, which causes a downward force on the droplet, leading to a decreased contact angle and a transition to a Wenzel wetting state. However, the droplets on square-pillar microstructured surfaces were observed sitting in the Cassie state, the observed superhydrophobic wetting state could be attributed to that the area fraction f on the square-pillar surface was largest in those four surfaces, that means the gravity of droplet on the space was less. This transition was not observed on the surfaces with same space between the pillars but higher pillar height (d=10 μm) since the vapor pressure may be increased by the higher pillars.

3.5 Conclusions

In this paper, the investigation of the wetting behavior of superhydrophobic surfaces with different micro-structures from 30 to 90 ℃ was described. The triangle, square, hexagon and circle four shapes micro-pillar surfaces with different wettability were successfully fabricated using the photolithography and ICP etching techniques. The contact angle on these 32-type micro-pillar surfaces were measurement and observed at different temperatures.

Contact angle measurements demonstrated the ability of the micro-pillar surfaces to form Cassie wetting states with a liquid droplet, most experimental surfaces sustaining large contact angles above 150◦. From this work, it was experimentally demonstrated the ability to turn an intrinsically hydrophilic silicon surface with very low contact angles (~40◦) to become superhydrophobic (>150◦) and turn back low contact angles (~40◦) with the specially appointed micro-pillar and surface temperature. Images obtained from the contact angle measurements indicated that liquid droplets sitting on the micro-pillar surfaces were in the Cassie–Baxter wetting state. The stability of this Cassie–Baxter state (superhydrophobic surfaces) could be increased by increasing the pillar height also could be decreased with increasing space between pillars and surface temperature. In addition, the wetting state could be transited from

Cassie–Baxter wetting state (superhydrophobic surfaces) to Wenzel wetting state (hydrophilic surfaces) with the higher temperature, lower pillar height and larger space between the pillars.

Chapter 4

Thermodynamic Analysis on Wetting Behavior of the Microstructured Surfaces

Abstract

Superhydrophobic surfaces had attracted much interest from experimental researches due to their special properties. Various researches to prepare these surfaces have been reported. However, the thermodynamic mechanisms of superhydrophobicity affected by surface roughness have not been understood completely. In this chapter, a 3-D square pillar-textured surface model was chosen to investigate the thermodynamic mechanism responsible for contact angle (CA), and free energy barrier (FEB). The effects of pillar width, space between pillars and pillar height on CA and FEB were obtained, and the calculated results are essentially consistent with the results of experimental measurement. The present approach could provide a theoretical guidance for designing superhydrophobic surfaces.

4.1 Introduction

As well known, the surface roughness may enhance wetting. Since Wenzel [42] first reported the effect of roughness, many studies of wetting have been reported. Kao [74] first reported an artificial superhydrophobic surface with contact angle (CA) higher than 150°. Subsequently, many methods for obtaining superhydrophobicity had been proposed and some studies had suggested criteria for achieving superhydrophobicity.

Superhydrophobic surfaces, which exhibit apparent contact angles (CA) greater than 150°and sliding angles lower than 10°[75, 76], had recently attracted significant attentions from both academic and industry because of their advantages, such as self-cleaning [5], oil repellency [77], water repellency [78].

Nature accomplished this fascinating property by developing special surface topography, and researchers had been uncovering myriad related morphological and physiological peculiarities of animals and plants [79-83, 84-87]. Subsequently, many methods investigating the relationship between surface topography and superhydrophobicity had been proposed and some of them had attempted to explain the underlying thermodynamic mechanism, such as Yamamoto, Li and Amirfazli [88–91].

However, most of these studies were inadequate for explaining the actual mechanism and no compared with the actual surfaces.

Meanwhile, numerous theoretical works based on 2-D thermodynamic analysis models have been made to investigate the superhydrophobicity. However, the 2-Dmodels had its limitation to deal with the complex situations, such as the pillar-textured surface with hexagon or triangular section shapes. Thus, it was worthwhile to study the superhydrophobicity using an advanced thermodynamic analysis model. Up to now, numerous researches had been reported to fabricate superhydrophobic surfaces by various methods with the development of Micro and Nano technology; it was achievable to prepare the ideal superhydrophobic surfaces by controlling their chemical composite and micro-nano hierarchical texture. However, in spite of significant advances in fabrication techniques for superhydrophobic surfaces, the effects of asperities on superhydrophobicity had not been fully understood. Therefore, considerable contributions had been made to put forward a criterion for superhydrophobicity

The surfaces contain square posts, hexagon posts, and triangle posts. Apparently, there were hardly any studies to provide the thermodynamic mechanisms for these unique surfaces. Therefore, the thermodynamic approached in predecessors' works using thermodynamic analysis of 3-D models were extend that could be applied to the pillar-textured surfaces with arbitrary cross-section shapes. The objective of the work reported in this paper was to resolve the issue of the thermodynamic mechanisms for any surface with complex microstructures. In order to show the validity of our approach, a square-section pillar-textured surface model is built as a typical example to compare the thermodynamic analysis with experimental results.

4.2 Theory and Calculation

The microstructured surface was pillar-textured surface in this research. The pillar width a, space between the pillars b, and the etching depth (pillar height) d were defined in Fig.4.1. The cross-section shapes of fabricated micro-pillar were square, triangle, and hexagon.

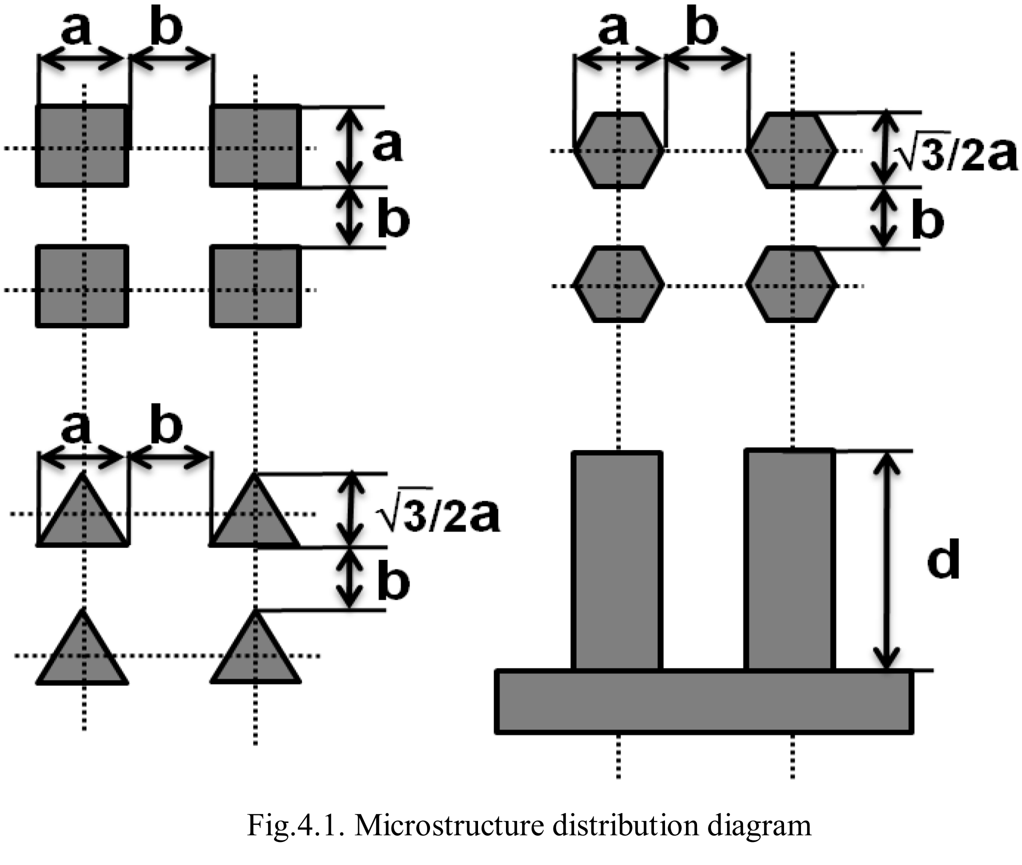

Fig.4.1. Microstructure distribution diagram

In this research, a method of thermodynamic analysis of a droplet on a pillar-textured surface using an idealized 3-Dmodel was used. To simplify the calculation, a square-section pillar-textured surface was considered as an example to show quantitative correlations between the geometrical parameters of the surface asperities and the thermodynamic concepts.

4.2.1 Basic Theory

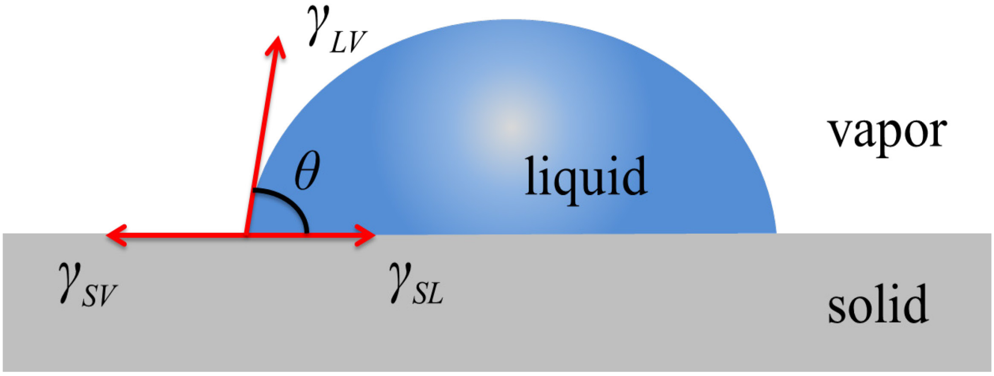

Fig.4.2. Illustration of the contact angle.

The first report of droplet contact angle on solid surfaces was published by Thomas Young [15]. Young's equation, which is suitable for the condition when a drop was placed on an ideal rigid, homogeneous, flat solid surface (as shown in Fig.4.2), can be expressed as

$$\cos\theta = (\gamma_{SV} - \gamma_{SL}) / \gamma_{LV} \qquad (4.1)$$

where γ_{SV}, γ_{SL} and γ_{LV}, were the surface tension coefficients on solid-vapor, solid-liquid, and liquid-vapor interfaces, respectively.

Both the Wenzel and Cassie-Baxter state has the following relation with the intrinsic contact angle θ and the topography of the roughness structure. Wenzel's theory described the non-composite state where water penetrates into the gap space when a droplet on a rough surface [42] (Fig.4.3).

$$\cos\theta w = r\cos\theta \tag{4.2}$$

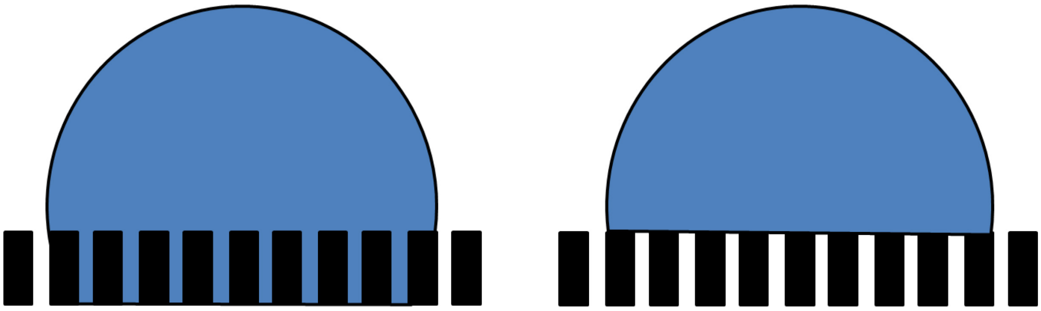

(a) Wenzel (composite) state (b) Cassie-Baxter (non-composite) state

Fig.4.3. States of droplets on the micro-structured surface.

Cassie's theory related to the composite state where the droplet on a rough surface traps air between solid and liquid. The wetting characteristic of such a surface was first addressed by Cassie and Baxter [43] and the apparent contact angle θc was predicted by the following equation.

$$\cos\theta_c = (\gamma^*_{SV} - \gamma^*_{SL})/\gamma_{LV} \tag{4.3}$$

where $\gamma^*_{SV} = f\,\gamma_{SV}$ and $\gamma^*_{SL} = (1-f)\gamma_{LV} + f\,\gamma_{SL}$, f is the area fraction. Researchers considered the three-phase contact line tension on the liquid-vapor-solid phase boundary and presented a new model to predict the contact angle of a water droplet on a rough surface [66, 67, 92].

$$\cos\theta_c^* = -1 + (1+\cos\theta)(1 - -\lambda/(K(1+\cos\theta)\gamma_{LV}))f \tag{4.4}$$

where λ is the line tension and K is the influence coefficient of scale effect. It was clear that the surface roughness can greatly influence the behavior of water drop on solid surface. On one hand, rough-ness increases the surface area of the solid, which geometrically enhances hydrophobicity (non-composite regime). On the other hand, vapor can remain trapped below the drop, which also leads to a superhydrophobic behavior, because the drop sits partially on vapor (composite regime) [89].

4.2.2 Analysis for Non-composite State

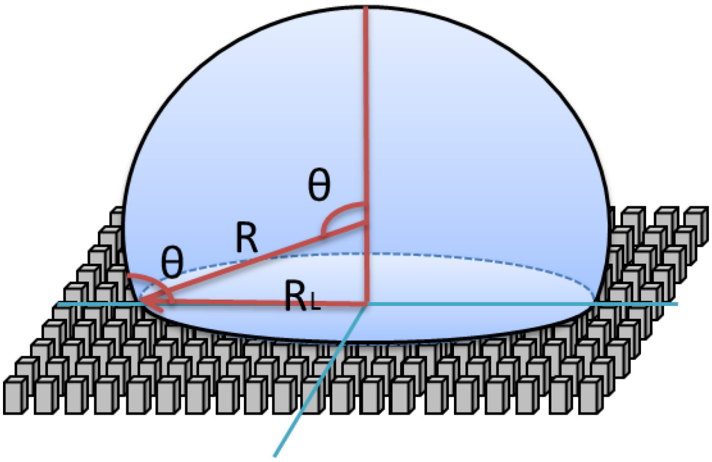

Fig.4.4. Water droplet on a square-pillar surface.

Some assumptions need to be made before the 3-D thermodynamic analysis. Three-phase contact line tension [93] and gravity were assumed to be neglected when the droplet was millimeter scale and droplet size was much larger than that of surface micro-texture. In every case, droplet surface was assumed to be spherical and the volume of droplet remains constant when three contact line moves.

In a 3-D system, the free energy (FE) of the system could be expressed as:

$$F= \gamma_{LV}S_{LV} + \gamma_{SL}S_{SL} + \gamma_{SV}S_{SV} \tag{4.5}$$

where S_{LV}, S_{SL} and S_{SV} were the liquid-vapor, solid-liquid and solid-vapor interface areas, respectively.

When the droplet volume and temperature were constant, the difference in the free energies of the contact lines at positions 1 and 2 was given by

$$\Delta F_{1\rightarrow 2}=F_2 - F_1$$

$$=\gamma_{LV}(S_{LV2} - S_{LV1})+ \gamma_{SL}(S_{SL2} - S_{SL1})+\gamma_{SV}(S_{SV2} - S_{SV1}) \tag{4.6}$$

where S_{LV}, S_{SL}, and S_{SV} were liquid–vapor, solid–liquid, and solid–vapor interface areas, respectively. Geometrically

$$S_{SL} + S_{SV}=C \tag{4.7}$$

The shift in the interface area from position 1 to position 2 could then be obtained as

$$S_{SL2} - S_{SL1}= S_{SV1} - S_{SV2} \tag{4.8}$$

Therefore, by combining these equation and Young's equation

$$\Delta F_{1\rightarrow 2}=\gamma_{LV}\{(S_{LV2} - S_{LV1}) - (S_{SL2} - S_{SL1}) \cos\theta \} \tag{4.9}$$

When a droplet on a rough surface, the external droplet surface area could be expressed as

$$S_{ext}= \frac{2\pi R_L^2}{1+cos\theta} \tag{4.10}$$

Where S_{ext} was the external droplet surface area, R_L was the radius of three-phase contact line. The radius of droplet R and volume of the droplet V in non-composite could be expressed as

$$R=R_L/\sin\theta \tag{4.11}$$

$$\frac{4}{3}\pi R^3 = \frac{\pi R_L^3}{sin^3\theta}\left\{(1-\cos\theta)-\frac{1}{3}(1-cos^3\theta)\right\}+\{\pi R_L^2-Na^2\}d \tag{4.12}$$

Where N was the number of pillars that were in contact with the droplet. Since the contact line between the three phases (vapor, liquid, and solid) moved to minimize the energy and stopped at the edges of the pillars, the actual contact lines were not circular but rather were as depicted in Fig.4.5. In the case of a composite state, the contact lines form two interfaces, namely a liquid–vapor interface and a solid–liquid interface.

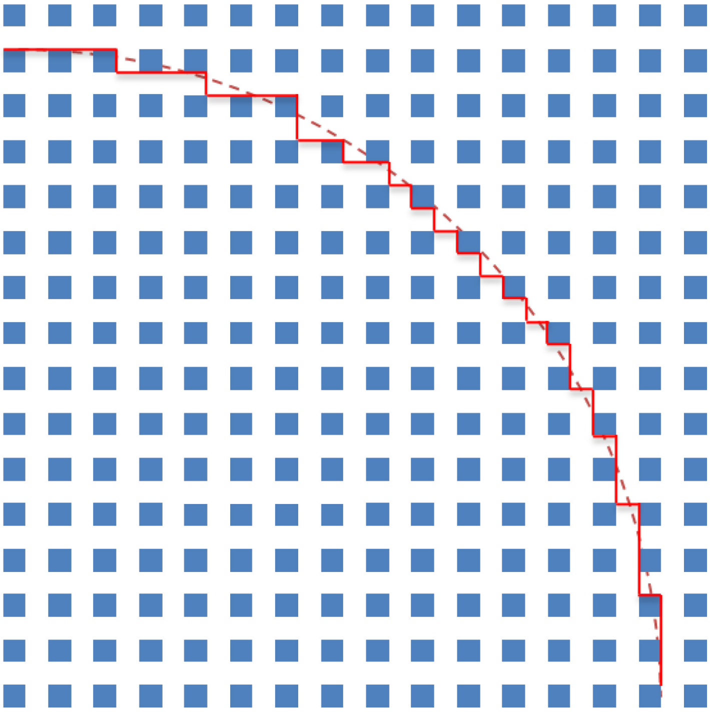

Fig.4.5. Actual contact line of a droplet

The system must overcome a free energy barrier (FEB) to move from one metastable state to another. To calculate the FEB, the relationship between FEB and surface geometrical configurations based on the unique properties of the actual three-phase contact line were established. Specifically, the FEB was split into receding FEB and advancing FEB, that were related to the actual three-phase contact line recedes from a single pillar and advances over the rest area of a repeated unit, respectively. The total area of a receding and an advancing was the area of were repeated unit. Here the states A, B, and C were taken as an example to show how the advancing or receding FE barriers.

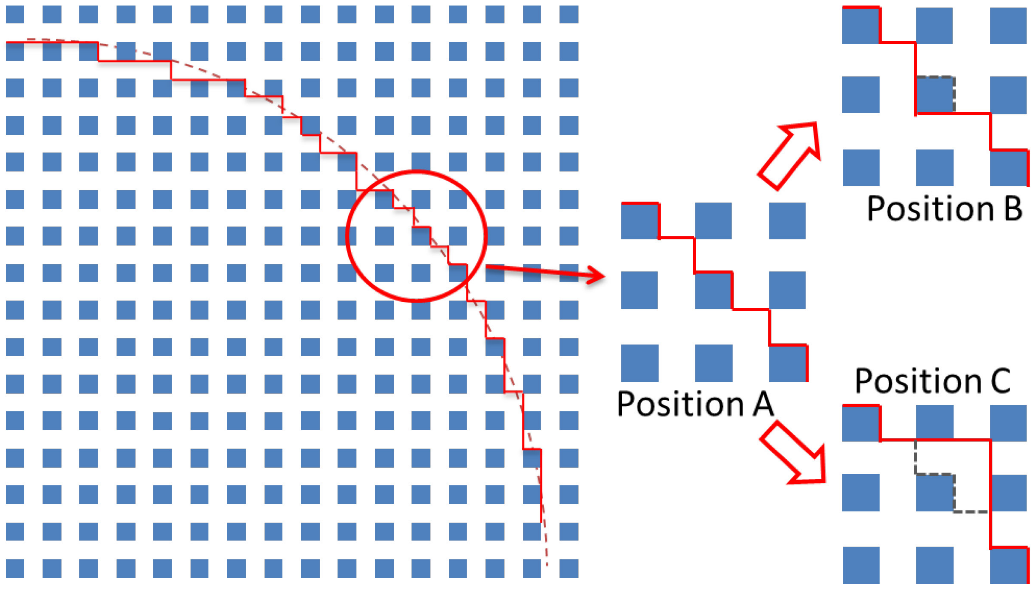

Fig.4.6. Illustration of wetting states from position A to B and C

Considering that the water drop receded from a preference position A with a CA θ_A to position B with a CA θ_B (see Fig.4.6), the change of the FE as a result of receding could be calculated using equation (4.8) :

$$\Delta F_{A\rightarrow B}=F_B-F_A$$

$$=\gamma_{LV}\{2\pi(\frac{R_{LB}^2}{1+cos\theta_B}-\frac{R_{LA}^2}{1+COS\theta_A})+a^2\cos\theta\} \qquad (4.13)$$

Because the volume of droplet remains unchanged, geometrically

$$\frac{\pi R_{LA}^3}{sin^3\theta_A}\left\{(1-\cos\theta_A)-\frac{1}{3}(1-cos^3\theta_A)\right\}$$

$$= \frac{\pi R_{LB}^3}{sin^3\theta_B}\left\{(1-\cos\theta_B)-\frac{1}{3}(1-cos^3\theta_B)\right\} \quad (4.14)$$

When the droplet advanced from state A to C, the change of the FE as a result of advancing can be calculated using equation (4.9) :

$\Delta F_{A\to C}=F_C-F_A$

$$=\gamma_{LV}\{2\pi(\frac{R_{LC}^2}{1+cos\theta_C}-\frac{R_{LA}^2}{1+COS\theta_A})+(b^2+2ab+4ad)\cos\theta\} \quad (4.15)$$

$$\frac{\pi R_{LA}^3}{sin^3\theta_A}\left\{(1-\cos\theta_A)-\frac{1}{3}(1-cos^3\theta_A)\right\}$$

$$=\frac{\pi R_{LC}^3}{sin^3\theta_C}\left\{(1-\cos\theta_C)-\frac{1}{3}(1-cos^3\theta_C)\right\}-(b^2+2ab)d \quad (4.16)$$

4.2.3 Analysis for Composite State

For the composite state, the same method could be used to obtain the corresponding parameters. For receding process, the corresponding equations could be expressed as

$\Delta F_{A\to B}=F_B-F_A$

$$=\gamma_{LV}\{2\pi(\frac{R_{LB}^2}{1+cos\theta_B}-\frac{R_{LA}^2}{1+COS\theta_A})+a^2\cos\theta\} \quad (4.17)$$

$$\frac{\pi R_{LA}^3}{sin^3\theta_A}\left\{(1-\cos\theta_A)-\frac{1}{3}(1-cos^3\theta_A)\right\}$$

$$=\frac{\pi R_{LB}^3}{sin^3\theta_B}\left\{(1-\cos\theta_B)-\frac{1}{3}(1-cos^3\theta_B)\right\} \quad (4.18)$$

For advancing process, the corresponding equations could be expressed as

$\Delta F_{A\to C}=F_C-F_A$

$$=\gamma_{LV}\{2\pi(\frac{R_{LC}^2}{1+cos\theta_C}-\frac{R_{LA}^2}{1+COS\theta_A})+(b^2+2ab)\cos\theta\} \quad (4.19)$$

$$\frac{\pi R_{LA}^3}{sin^3\theta_A}\left\{(1-\cos\theta_A)-\frac{1}{3}(1-cos^3\theta_A)\right\}$$
$$=\frac{\pi R_{LC}^3}{sin^3\theta_C}\left\{(1-\cos\theta_C)-\frac{1}{3}(1-cos^3\theta_C)\right\} \quad (4.20)$$

4.3 Results and Discussion

According to the previous analysis, the parameters of the surface microstructure affect the system free energy barrier, which affects the contact angle.

4.3.1 Effect of Pillar Height

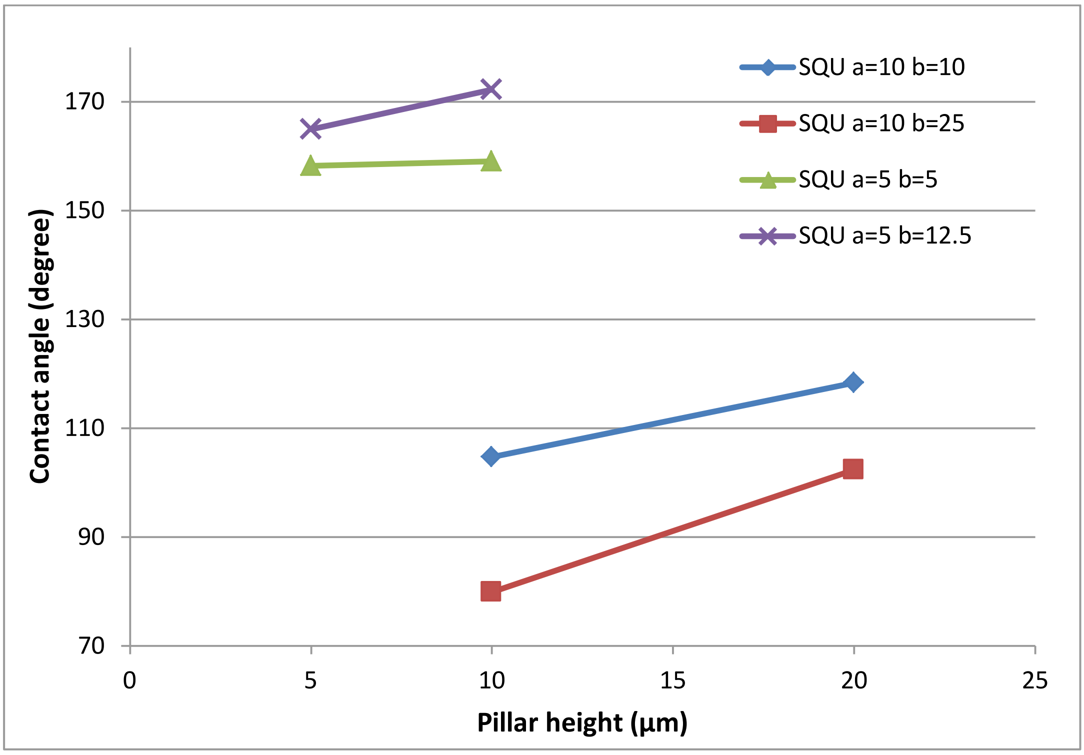

Fig.4.7. Effect of the pillar height on non-composite state

Fig.4.7 indicated the effect of pillar height d on the non-composite state for constant a and b. When the pillar height increased, the CA increased.

4.3.2 Effect of Pillar Width

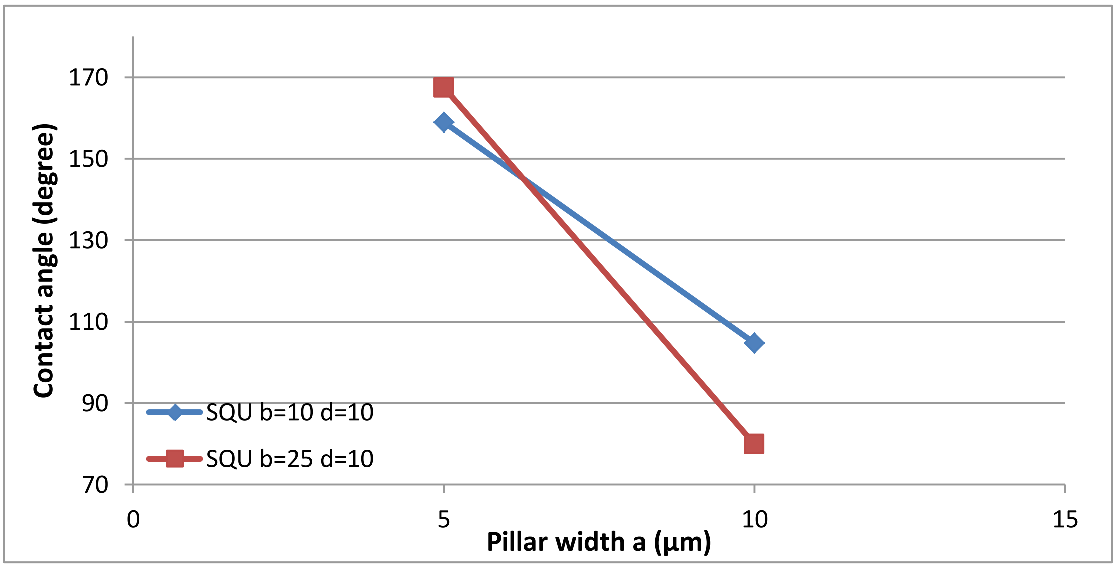

Fig.4.8. Effect of the pillar width

Fig.4.8 indicated the effect of pillar width a on the micro-pillar surface for constant b and d. In contrast to space between pillars, varying the pillar width has strongly effect on the CA. The CA decreased steep with an increase in the pillar width.

4.3.3 Effect of Space between Pillars

Fig.4.9 indicated the effect of space between pillars b, on the non-composite state for constant a and d. A wider space caused the CA to increase on the non-composite state and to decrease on surface with pillar width a=10 µm because of the state transition when increase the space between the pillars.

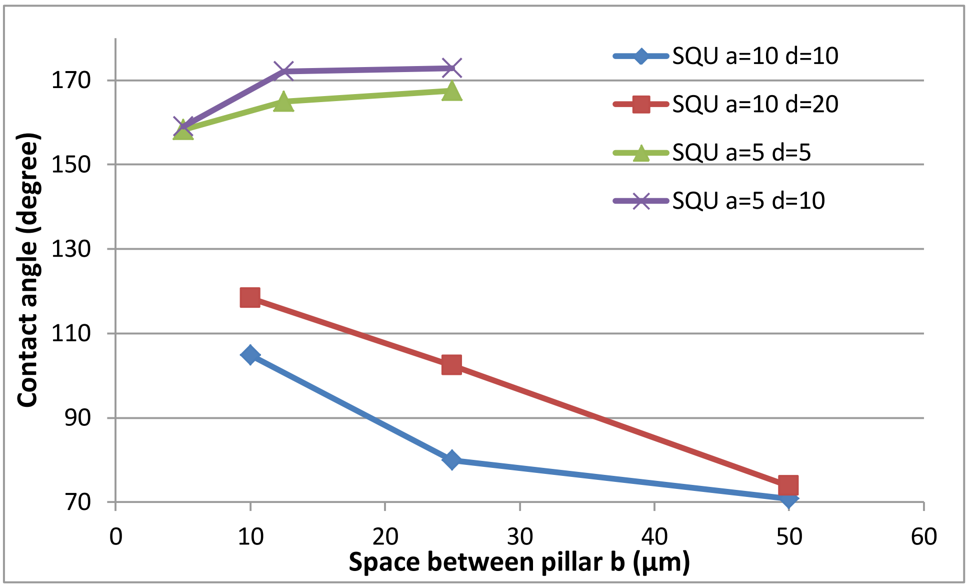

Fig.4.9. Effect of space between pillars

4.3.4 Scale Effect

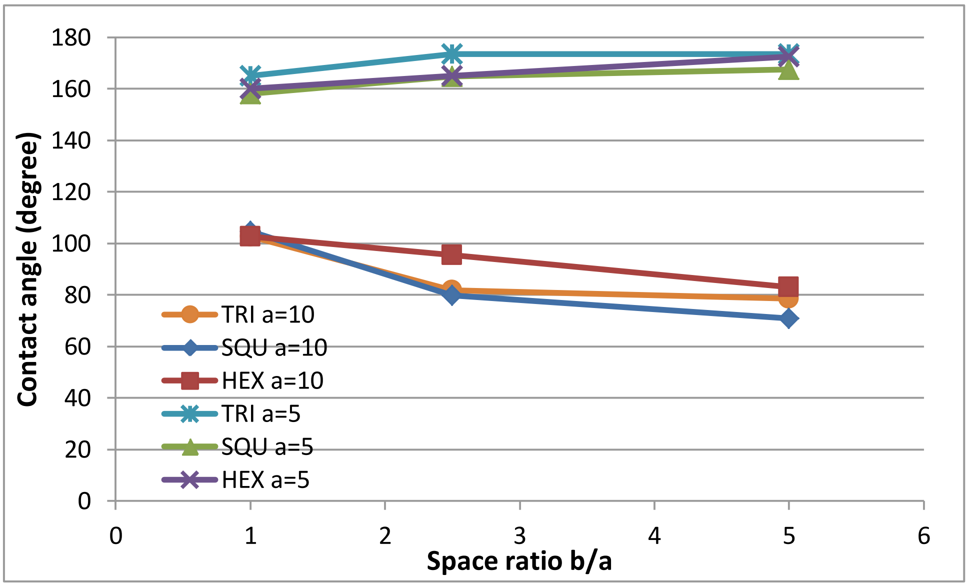

Fig.4.10. Scale effect on micro-pillar surfaces

Changing scale with the same rate of a, b, and d might change the character of surfaces. Fig.4.10 indicated the CA curves of two scales on the triangle-, square-, and hexagon-pillar surfaces. Those two scales CA curves were not the same shape because the different wettability on these two surface. Wettability on micro-pillar surface with pillar width a=5 μm was superhydrophobicity, however on the micro-pillar surface with pillar width a=10 μm was transited from hydrophobic to hydrophilic when the space ratio increased.

4.4 Conclusions

A thermodynamic analysis of 3-D models had been proposed to investigate the superhydrophobic behavior for pillar-textured surfaces. Based on the characteristics of actual three-phase contact line and the repeated unit, FEB was split into the two parts responsible for advancing and receding FEBs. The results obtained by this approach were fairly consistent with the results of theoretical calculations and experimental measurement. More importantly, the thermodynamic approaches in predecessors' works were extended to any pillar-textured surface with complex cross-section shapes. It was interesting to note that for a given texture structure, height plays an important role in superhydrophobicity. Equilibrium CA of non-composite state increased with pillar height and space between pillars increased. The results can be used for fabricating superhydrophobic surfaces. This approach is also expected to be extendable to hierarchical structured superhydrophobic surfaces.

Chapter 5

The Droplet Rebound Temperature on the Microstructure surfaces

Abstract

Two series of microstructured silicon surfaces which was decorated by micro-pillars whose pillar width, space between pillars and pillar height can be adjusted independently were fabricated. These surfaces possessed a hydrophobic/superhydrophobic property. The dynamic behavior and rebound temperature of water droplets impacting these structured surfaces was examined using a high-speed camera. Experimental results validated that the difference in the droplet rebound temperature was subjected to the solid fraction referred to as the ratio of the actual area contacting with the liquid to its projected area on the textured surface, because the mechanism by which the residual liquid film emerges on the pillars' tops could essentially be ascribed to the pinch-off of the liquid threads.

5.1 Introduction

With the discovery of novel wetting phenomena in nature, such as the self-cleaning effect of lotus leaves and the effortless stand and quick waterborne movement of water striders legs, surfaces with special wettability had recently attracted significant attention and had become increasingly important in our daily lives.[94-98] Moreover, surface wettability at non-ambient temperature, especially at high temperature (above 100℃), was of great importance in many industrial processes, including water transportation and metal processing, among others [38,39].

Central to many technological processes such as spray cooling and fuel injection in combustion engines was the phenomenon of individual droplets impacting on superheated surfaces.[99,100] Recently, several advances have been made, such as the fabrication of thermally responsive materials with controllable wettability,[58] the repellent characteristics of different superhydrophobic surfaces to hot water,[56] application of hydrophobic surfaces on heat exchangers at low temperature,[63] evaporation-triggered wetting transition for water droplets on hydrophobic microstructures,[62] and enhancement of boiling by nanostructured interfaces.[101] However, the effect of surface morphology on the wetting behavior at high temperature had not been studied systematically.

The goal of these processes was to enhance the heat transfer rate between the liquid and the solid surface.[100] Effective heat transfer requires that the liquid came into contact with the solid surface upon impact (the contact boiling regime). However, contact was only possible as long as the hot surface temperature was lower than a critical value, the rebound temperature.[55] A liquid drop impacting on a solid substrate can originate a large variety of outcomes, among which one of the most spectacular is drop rebound. The minimum surface temperature at which a droplet can be bounced is called the rebound temperature. Beyond this temperature, the liquid remained separated from the hot solid surface by a developing vapor layer. In this so-called film boiling regime, the vapor layer, due to its poor thermal conductivity, drastically reduced the heat transfer between the liquid and the solid and potentially risked surface overheating and equipment burnout. As a result, studies of heat transfer enhancement could not be separated from those of the rebound temperature, especially in the context of droplet impact on superheated surfaces.

Herein, the wetting behavior of surfaces with different structures at high temperature was investigated. Varied kinds of micro-structured surfaces with different wettability were successfully fabricated. The wetting behavior of a water droplet was observed to be different on the surfaces, and the wetting transition (from spreading to rebounding) occurred at a specific temperature (i.e., the rebound temperature, Tr) on these fabricated surfaces. Surface wettability was crucial to the wetting-transition behavior, and surface roughness also affected the rebound temperature of a surface (Tr). When surfaces with the same chemical composition, Tr decreased with the pillar width decreased, and increased with the space between pillars increased.

5.2 Experimental Methods

5.2.1 Surface Preparing and Measurements

These micro-pillars were uniformly distributed in a square grid on a glass mask. Before the fabricating process, a 400 μm thick 4 inch Silicon wafer ((100), p-type) was cleaned in RCA process rinsed by the DI water and dry, then a 1.5 μm positive photoresist layer (s1815) was spinning-coated on the Si surface. In the next step, the required pattern was transferred from the mask to the photoresist layer by UV exposing; subsequently the photoresist was partly removed by the developer. The uncovered Si was etched in the ICP etcher (STS MC21) to finally fabricate the roughness pattern on the Si wafer.

The micro-pillar surfaces used in research were 10um-level triangle-, square-, and hexagon-pillars surfaces, and 5um-level triangle-, square-, hexagon-, and circle-pillars surfaces(as shown in the Fig.5.1). The space ratio b/a was 1, 2.5 and 5 for 10um-level surfaces and 1, 2.5, 5 and 10 for

5um-level surfaces. The heights of pillar d=a and d= 2a.

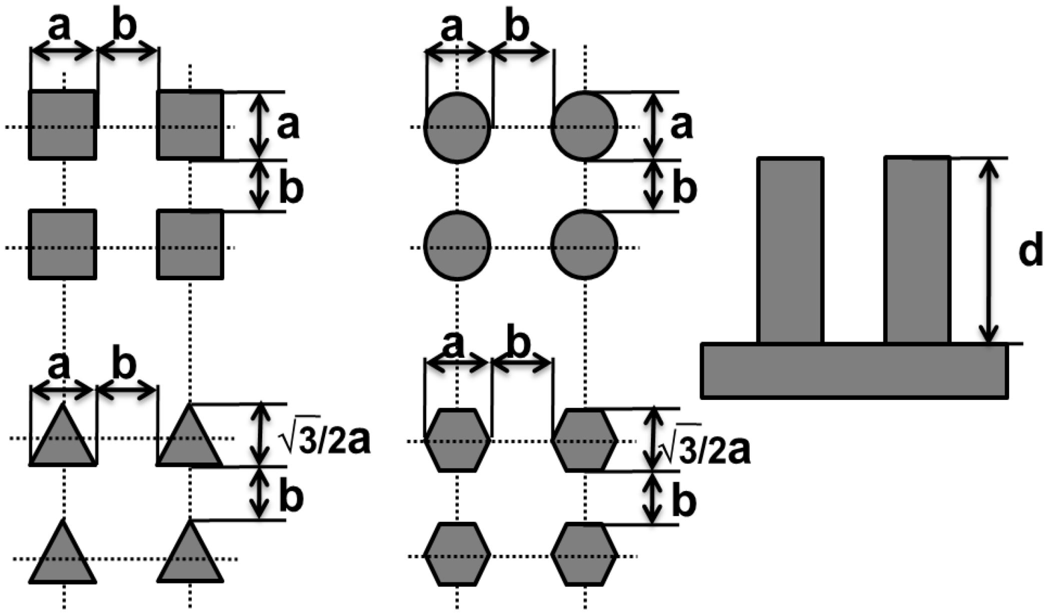

Fig.5.1. Microstructure distribution diagram

5.2.2 High Speed Camera

A heating stage with controllable temperature was used. The surface temperature and the water spreading or rebounding were recorded with a precise thermocouple and a CCD, respectively. The injector was kept 20 mm higher than the heating surfaces to preserve the drop from heat. A 10 μL DI water droplet was pushed out. The water droplet was well preserved before coming into contact with the high-temperature surfaces.

A Digital camera with high-speed model (Nikon1 J5) was employed to record the spreading and rebounding processes of impacting droplets from the side. From the side-view recording of each impact experiment, the droplet rebound temperatures Tr were measure.

5.3 Results and Discussions

Typically, the behaviors of droplets during impact on superheated surfaces could be specified as contact boiling or film boiling. Depending on the temperature of the solid surface, the liquid may display boiling characteristics from mild bubble formation to vigorous bubble expansion and droplet ejection. Increasing the surface temperature induced more and more vapor to be generated between the liquid and the solid surfaces, which hindered the heat transfer rate. If the surface temperature was further increased beyond a critical point, a vapor layer developed and prevented the liquid from making any contact with the solid surface, and the impact was said to be in the film boiling regime.

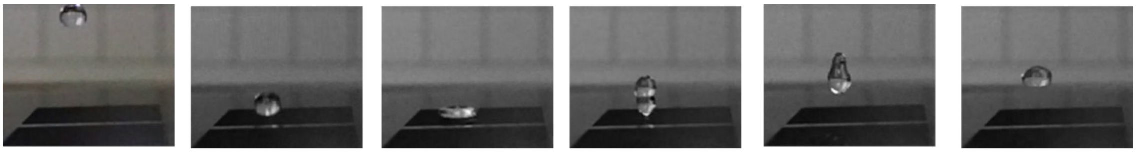

(a) 0s 4.2ms 15.0ms 29.2ms 37.5ms

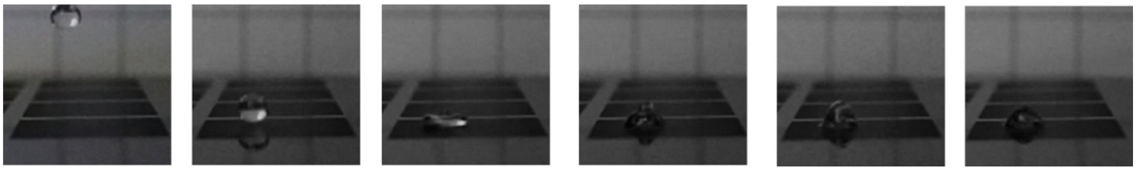

(b) 0s 4.2ms 9.2ms 13.3ms 15.8ms

Fig.5.2 Droplet impact on the heated surface.

(a) surface temperature >Tr, (b) surface temperature <Tr

Fig.5.2 showed the droplet impact process on micro-pillar surfaces. The droplet was spread to maximum at 4.2 ms and then rebounded on surface with temperature was higher than the rebound temperature. The rebounded droplet got the highest position at 37.5 ms, and the height to the surface was 3.3mm (as shown in Fig.5.2 (a)). The droplet impact on the surface which temperature was lower than rebound temperature, the droplet was spread to maximum at 4.2 ms and then shook on the surface. The shaken droplet got the highest position at 13.3 ms (as shown in Fig.5.2 (b)).

5.3.1 Profile Characterization Effect

Fig.5.3 indicated the rebound temperature on the triangle-pillar surfaces. As shown in the Tr curve, for the contrast pillar width a, the rebound temperature on the triangle pillar surfaces increased with the space ratio (b/a) and decreased with the pillar height increased, and for the contrast space ratio b/a, the rebound temperature decreased with pillar width a decreased and pillar height d increased. when the space ratio b/a=5, the Tr on the surface with pillar width a=5μm (254.8 ℃) was higher than the Tr on the surface with pillar width a=10 μm (248.1 ℃).

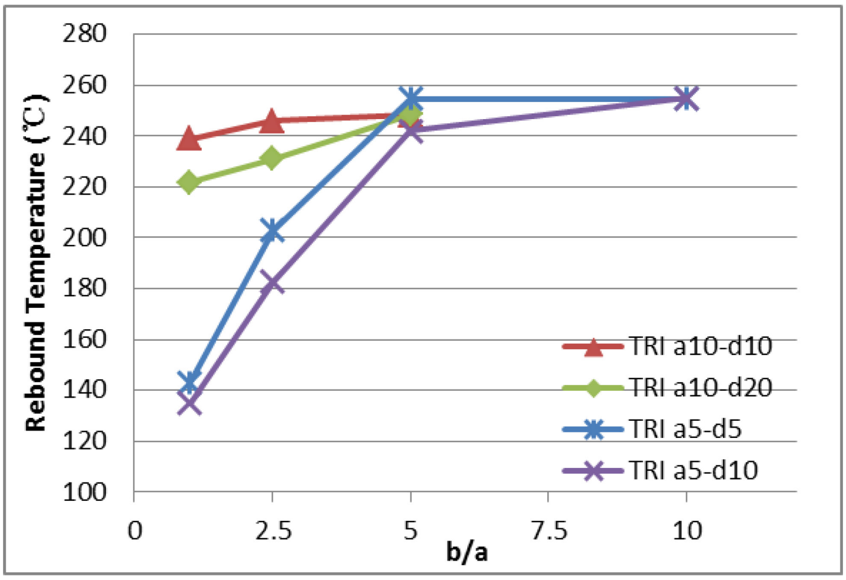

Fig.5.3. Rebound temperature on the triangle-pillar surfaces

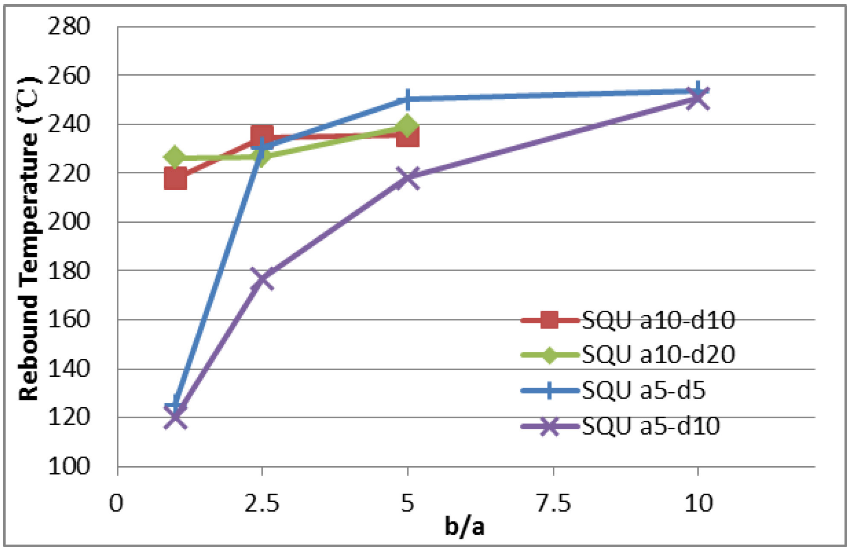

Fig.5.4. Rebound temperature on the square-pillar surfaces

Fig.5.4 indicated the rebound temperature on the square-pillar surfaces. The Tr curve showed the similar change rules on the triangle-pillar surface. when the space ratio b/a=2.5, the Tr on the surface with pillar width a=5 μm (230.6 ℃) approximated to the Tr on the surface with pillar width a=10 μm (234.8 ℃). when the space ratio b/a=5, the Tr on the surface with pillar width a=5 μm (250.2 ℃) was higher than the Tr on the surface with pillar width a=10 μm (235.6 ℃).

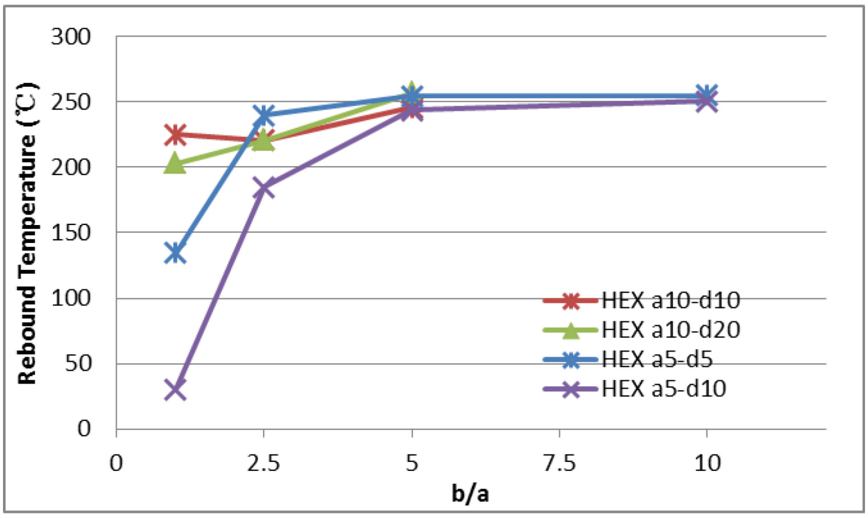

Fig.5.5. Rebound temperature on the hexagon-pillar surfaces

Fig.5.5 indicated the rebound temperature on the hexagon-pillar surfaces. The Tr curve showed the similar change rules on the other two surfaces. when the space ratio b/a=2.5, the Tr on the surface with pillar width a=5 μm (239.9 ℃) was higher than the Tr on the surface with pillar width a=10 μm (220.7 ℃). The droplet was rebounded on the surface with pillar width a= 5um, space between pillar b=5 μm, and pillar height d=5 μm at room temperature since the superhydrophobic wettability and relative smoother pillar edge line.

Although substrates with similar structures, exhibited similar high temperature spreading and rebounding and had similar contact times in the bouncing process, Tr of surfaces with similar contact angles varied with the change of surface roughness. Fig5..2, Fig.5.3, and Fig.5.4 showed the relationship between surface roughness and Tr for triangle-, square- and hexagon-pillar surface. When the pillar height h=a, with an increased in space ratio b/a (from 1 to 5 for surfaces with pillar width a =10 μm and from 1 to 10 for surfaces with pillar width a =10 μm) Tr increased for the triangle-pillar surface (from 238.8 to 248.1℃ when a=10 μm, and from 142.9 to 254.7 ℃ when a=5 μm) while it also increased for the square-pillar surface (from 217.8 to 235.6 ℃ when a=10 μm, and from 125.1 to 253.5 ℃ when a=5 μm) and hexagon-pillar surfaces (from 225.2 to 245.5 ℃ when a=10 μm, and from room temperature 28 to 255.1 ℃ when a=5 μm).

At a given temperature, the vaporizing velocity of a droplet clearly depended on the heat-transfer ability of the surface. The more heat was transferred through the solid–liquid interface, the faster the droplet vaporized. Hence, the wetting and rebounding processes both indicated that the hydrophilic surface had excellent heat-transfer ability. The drop evaporated very fast below Tr, and above Tr, the bottom part of the droplet evaporated faster and formed a vapor film to rebound the droplet up. In comparison, the droplet stood on the superhydrophobic surface with a contact angle larger than 150° and evaporated very slowly at lower temperature and did not wet but rebound or rolled away. The small velocity of vaporization demonstrated the poor heat-transfer ability of the superhydrophobic surface.

5.3.2 Shape Effect

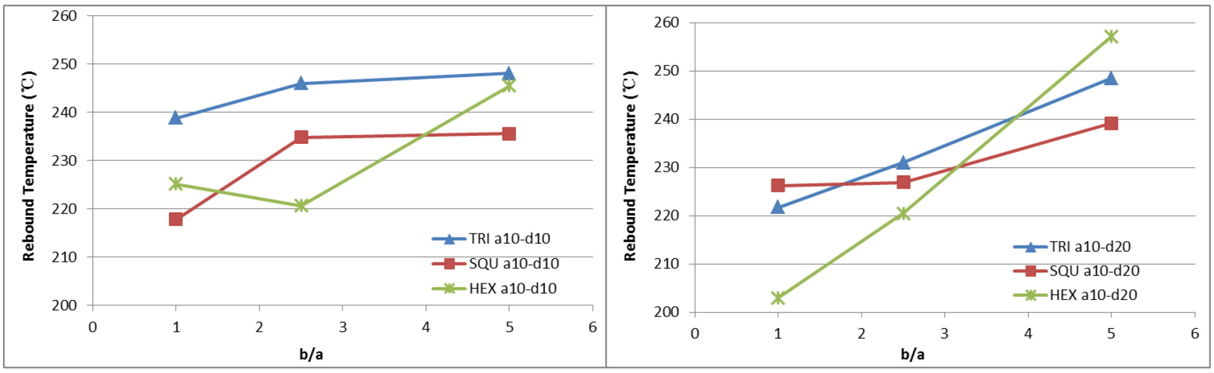

(a)Pillar height d=10 (b) Pillar height d=20

Fig.5.6 Tr on the micro-pillar surfaces with pillar width a = 10 um.

Fig.5.6 (a) and (b) indicated the Tr on the triangle- square- and hexagon-pillar surfaces with pillar width a = 10 μm. Fig.5.6 (a) describe the Tr on these surfaces with pillar height d= 10 μm, the Tr on the triangle- pillar surface was higher than other 2 shapes surfaces. The Tr on the triangle- and square-pillar surfaces started steep and later flattened with the space between pillars increased. However, the Tr on the hexagon-pillar surfaces decreased first and then increased with the space between pillars increased. When the pillar height d=20 μm, the Tr curves increased lineally with the space between pillars increased (as shown in Fig.5.6 (b)).

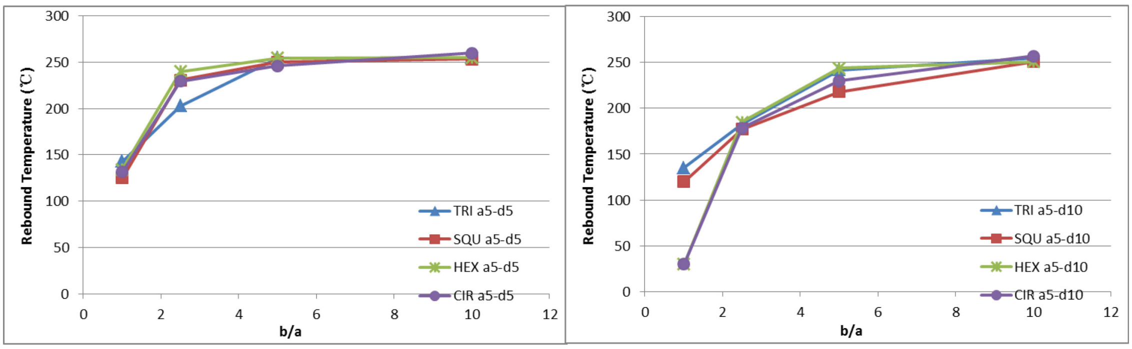

(a)Pillar height d=5 (b) Pillar height d=10

Fig.5.7. Tr on micro-pillar surfaces with pillar width a = 5 um

For the 5-μm-level micro-pillar surfaces, four shapes micro-pillar surfaces were fabricated with varied spaces between pillars. Fig.5.7 (a) and (b) indicated the Tr on the triangle-, square-, hexagon-, and circle pillar surfaces with pillar width a = 5 μm and pillar height d= 5 &10 μm. All the Tr curves on four shape micro-pillar surfaces started stead and steep and later flattened with the space between pillars increased. When the pillar height d= 5 μm, The lowest Tr on these surfaces was 125.1 ℃ on the square-pillar surface when space between pillars b=5 μm. however, the droplets were rebound on the hexagon- and circle-pillar with pillar height d=10 μm at room temperature (28 ℃) since the superhydrophobic wettability and relative smoother pillar edge line.

The comparisons between the Tr of different surfaces remind that, although the hydrophilic could enhance heat transfer between solid and water, the droplet would rebound on them at a lower temperature compared with the hydrophilic surface. Furthermore, if the surface temperature is above Tr, a vapor film would be generated. Therefore, for equipment with strict and high working temperature, the surface with a higher Tr should be chosen.

5.4 Conclusions

In this research, the typical wetting transition on microstructured surfaces with different wettabilities at high temperature had been investigated. Experimental results indicate that both surface wettability and surface roughness are crucial to the wetting transition behavior. The spreading–rebounding transition occurred on hydrophobic (surface with pillar width a=10 μm) and superhydrophobic surfaces. When the side length of micro-pillars on substrates decreased from 10 μm to 5 μm, rebound temperature decreased for the superhydrophobic micro-pillar surfaces, especially, the droplet was rebounded on the hexagon- and circle-pillar surface (HEX a5-b5-d10 and CIR a5-b5-d10) at room temperature. Moreover, the high-temperature wetting transition could be potentially valuable in water transportation and other industrial applications, such as material choice in liquid–solid systems working at non-ambient temperature.

Chapter 6

Outlook

Abstract

The subject of this thesis was investigation on the wettability and droplet impact on the heated micro-pillar structured surfaces. The aim was to obtain controllable wettability on Si based microstructured surfaces at different surface temperature. An outlook was formulated in this chapter.

6.1 General Recommendations and Outlook

1. Although various micro-pillar surfaces were fabricated and investigated in this research, but the sample variety was still not sufficient for the systematic research of wettability on the microstructured surface. The temperature effect was described on the hydrophobic and super hydrophobic surfaces; however, the theory of temperature effect was not investigated deeply. Further experimental investigation and theory analysis could improve and perfect the research of wettability on the microstructured surface with different temperature.

2. In this research, three-phase contact line tension and gravity were assumed to be neglected in the thermodynamic analysis. But with the microstructures becoming smaller and smaller, the three-phase contact line tension effect could not be neglected summarily. Further theoretical investigation of thermodynamic analysis will include more actual mechanisms for any microstructured surfaces.

3. Impacting droplets on superheated microstructured surfaces at various Weber and Reynolds number may result in a wealth of phenomena, including jet formation, micro-droplet formation, splashing. Further experimental investigation of the dynamics after droplet impact, will certainly result in new and exciting fundamental discoveries and are highly relevant for industrial applications like inkjet printing, spray cooling and spray painting.

References

[1] K.N. Prabhu, P. Fernandes, G. Kumar. Effect of substrate surface roughness on wetting behaviour of vegetable oilsMater. Des. (2009) vol.30, 2, 297-305

[2] P. Andersson, J. Koskinen, S. Varjus, etal. Micro lubrication effect by laser-textured steel surface, Wear, (2007) 262, 369-379.

[3] Y.Q.Wang, H.F. Yang, Q.G. Hang, L. Fang, S.R. Ge. Tribological and lubrication properties of sandblast-textured surfaces with varied roughness Adv.Mater. Res. (2010) 154–155, 1019-1022

[4] M. Sakai, T. Yanagisawa, A. Nakajima, Y. Kameshima, K. Okada. Effect of surface structure on the sustainability of an air layer on superhydrophobic coatings in a water-ethanol mixture. Langmuir (2009) 25, 13-16

[5] L. Feng, S. Li, Y. Li, H. Li, L. Zhang, J. Zhai, Y. Song, B. Liu, L. Jiang, and D. Zhu, Super-Hydrophobic Surfaces: From Natural to Artificial, Adv. Mater. (2002) 14, 1857-1860.

[6] X.F. Gao, L. Jiang, Water-repellent legs of water striders, Nature (2004) 432, 36.

[7] Y. Zheng, X. Gao, and L. Jiang, Directional adhesion of superhydrophobic butterfly wings , Soft Matter (2007) 3, 178-182.

[8] X. Gao, X. Yan, X. Yao, L. Xu, K. Zhang, J. Zhang, B. Yang, and L. Jiang, The Dry-Style Antifogging Properties of Mosquito Compound Eyes and Artificial Analogues Prepared by Soft Lithography, Adv. Mater. (2007) 19, 2213-2217.

[9] A. R. Parker and C. R. Lawrence, Water capture by a desert beetle, Nature (2001) 414, 33-34.

[10] Y. Zheng, H. Bai, Z. Huang, X. Tian, F.-Q. Nie, Y. Zhao, J. Zhai, and L. Jiang, Directional water collection on wetted spider silk , Nature (2010) 463, 640-643.

[11] M. Liu, S. Wang, Z. Wei, Y. Song, and L. Jiang, Bioinspired Design of a Superoleophobic and Low Adhesive Water/Solid Interface , Adv. Mater. (2009) 21, 665-669.

[12] M. R. Flynn and J. W. M. Bush, Underwater breathing: the mechanics of plastron respiration , J. Fluid Mech. (2008) 608, 275-296.

[13] D. Quéré, Wetting and Roughness , Annu. Rev. Mater. Res. (2008) 38, 71-99.

[14] Srinivasarao M. Nano-Optics in the Biological World: Beetles, Butterflies, Birds, and Moths. Chem Rev. (1999) 99, 1935-1962.

[15] T. Young. An essay on the cohesion of fluids. Philosophical Transactions of the Royal Society of London, (1805) 95, 65–87.

[16] H. Yang, P. Jiang. Self-Cleaning Diffractive Macroporous Films by Doctor Blade Coating. Langmuir (2010) 26, 12598-12604.

[17] B. Bhushan, Y.C. Jung, K. Koch. Self-Cleaning Efficiency of Artificial Superhydrophobic Surfaces. Langmuir (2009) 25, 3240-3348.

[18] M. Rauscher, S. Dietrich. Wetting phenomena in nanofluidics. Annu. Rev. Mater. Sci. (2008) 38, 143-172.

[19] K. Fei, C.P. Chiu, C.W. Hong, Molecular dynamics prediction of nanofluidic contact angle offset by an AFM. Microfluid. Nanofluid. (2008) 4, 321-330.

[20] Z. Keshavarz-Motamed, L. Kadem, A. Dolatabadi, Effects of dynamic contact angle on numerical modeling of electrowetting in parallel plate microchannels. Microfluid. Nanofluid. (2010) 8, 47-56.

[21] C.-J. Chang, C.-F. Wang, J.-K. Chen, C.-C. Hsieh, P.-A. Chen. Fast formation of hydrophilic and reactive polymer micropatterns by photocatalyticlithography method. Appl. Surf. Sci. (2013) 286, 280–286.

[22] A. Haghdoost, R. Pitchumani. Fabricating superhydrophobic surfaces via a two-step electrodeposition technique. Langmuir (2013) 30, 4183–4191.

[23] N. Wang, D. Xiong, Influence of trimethylethoxysilane on the wettingbehavior, humidity resistance and transparency of tetraethylorthosilicatebased films, Appl. Surf. Sci. (2014) 292, 68–73.

[24] M. Pei, B. Wang, Y. Tang, X. Song, H. Yan, X. Zhang. Fabrication of superhydrophobic copper surface by direct current sputtering and its underwater stability. Thin Solid Films (2013) 548, 313–316.

[25] E. Jenner, C. Barbier, B. D'Urso. Durability of hydrophobic coatings for superhydrophobic aluminum oxide. Appl. Surf. Sci. (2013) 282, 73–76.

[26] Y.Y. Yan, N. Gao, W. Barthlott, Mimicking natural superhydrophobic surfacesand grasping the wetting process: a review on recent progress in preparingsuperhydrophobic surfaces, Adv. Colloid Interface Sci. (2011) 169,80–105.

[27] Yutaku Kita, Coinneach Mackenzie Dover, Alexandros Askounis, Yasuyuki Takata and Khellil Sefiane, Drop mobility on superhydrophobic microstructured surfaces with wettability contrasts, Soft Matter, 2018, 14, 9418-9424

[28] Periklis Papadopoulos, Bat-El Pinchasik, Martin Tress, Doris Vollmer, Michael Kappl and Hans-Jurgen Butt, Wetting of soft superhydrophobic micropillar arrays, Soft Matter, 2018, 14, 7429-7434

[29] Nan Wang, Dangsheng Xiong, Mengtong Li, Yaling Deng, Yan Shi,Kun Wang, Superhydrophobic surface on steel substrate and its anti-icing property in condensing conditions, Applied Surface Science (2015) 355, 226–232

[30] A. Susarrey-Arce, Á. G. Mańin, H. Nair, L. Lefferts, J. G. E. Gardeniers, D. Lohse and A.van Houselt. Absence of an evaporation-driven wetting transition on omniphobic surfaces. Soft Matter (2012) 8, 9765-9770

[31] H. Ems, S. Ndao. Microstructure-alone induced transition from hydrophilic to hydrophobic wetting state on silicon. Applied Surface Science (2015) 339, 137–143

[32] D. Zong; Z. Yang; and Y. Duan. Dynamic spreading of droplets on lyophilic micropillar-arrayed Surfaces. Langmuir, (2018) 34, 4417-4425.

[33] S. Qiao; S. Li; Q. Li; B. Li; K. Liu; and X. Feng. Friction of droplets sliding on microstructured superhydrophobic surfaces. Langmuir, (2017) 33, 13480-13489.

[34] ZHENG QuanShui, et al. Small is beautiful, and dry. Sci China Phys Mech Astron December (2010) 53, 12, 2245-2259

[35]Baldacchini T, Care J E, Zhou M, Mazur E. Superhydrophobic surfaces prepared by microstructuring of silicon using a femtosecond laser. Langmuir, (2006) 22, 4917.

[36]Oner D, McCarthy T J. Ultrahydrophobic surfaces. Effects of topography length scales on wettability. Langmuir, (2000) 16, 7777.

[37]Zhao H, Law K Y. Directional Self-Cleaning Superoleophobic Surface. Langmuir,

(2012), 28, 11812

[38]. J. Hashim, L. Looney, M. S. J. Hashmi. The wettability of SiC particles by molten aluminium alloy. J. Mater. Process. Technol. (2001) 119, 324 – 328.

[39] J. Hashim, L. Looney, M. S. J. Hashmi, J. Mater. The enhancement of wettability of SiC particles in cast aluminium matrix composites. J. Mater. Process. Technol. (2001) 119, 329 – 335.

[40] A.W. Neumann. Contact angles and their temperature dependence: thermodynamic status, measurement, interpretation and application. Adv. Colloid Interface Sci. (1974) 4, 105-191

[41] D. Li, A.W. Neumann. in Applied Surface Thermodynamics. ed. by J.K. Spelt, A.W. Neumann (Dekker, New York, 1996), p. 109

[42] RN. Wenzel. Resistance of solid surfaces to wetting by water. Ind. Eng. Chem. (1936) 28, 988

[43] A. B. D Cassie and S. Baxter. Wettability of porous surfaces. Trans. Faraday Soc. 40, 546, (1994).

[44] A. Marmur. Wetting on hydrophobic rough surfaces: to be heterogeneous ornot to be? Langmuir (2003) 19, 8343–8348.

[45].M. Li, W. H. Li, J. Zhang, G. Alici, and W. Wen. A review of microfabrication techniques and dielectrophoretic microdevices for particle manipulation and separation, J. Phys. D. Appl. Phys. (2014) 47, 063001.

[46]. Method of anisotropically etching silicon. United States Patent 5501893

[47]T. Marik. study and applications of liquid behavior on microtextured solid surfaces. phD thesis, University of Illinois at Urbana Champaign. (2011)

[48]R. Tadmor; R. Das; S. Gulec; J. Liu; H. E. N'guessan; M. Shah; P. S. Wasnik, and S. B. Yadav. Solid-liquid work of adhesion. Langmuir (2017) 33, 3594-3600.

[49]Y. Zheng; X. Gao; and L. Jiang. Directional Adhesion of Superhydrophobic Butterfly Wings. Soft Matter (2007) 3(2), 178-182.

[50]X. Gao; X. Yan;, X. Yao; L. Xu; K. Zhang; J. Zhang; B. Yang; L. Jiang. The Dry - Style Antifogging Properties of Mosquito Compound Eyes and Artificial

Analogues Prepared by Soft Lithography. Adv. Mater. (2007)19, 2213-2217.

[51]Yongmei Zheng; Hao Bai; Zhongbing Huang; Xuelin Tian; Fu-Qiang Nie; Yong Zhao; Jin Zhai; Lei Jiang. Directional water collection on wetted spider silk. Nature (2010) 463, 640-643.

[52]Jiayu Wang; Minh Do-Quang;, James J. Cannon; Feng Yue; Yuji Suzuki; Gustav Amberg; Junichiro Shiomi. Surface structure determines dynamic wetting. Scientific Reports, (2015) 5, 8474.

[53]W. Fang; H. Guo; B. Li, Q. Li; and X. Feng. Revisiting the critical condition for the cassie–wenzel transition on micropillar-structured surfaces. Langmuir (2018) 34, 3838-3844.

[54] K. Yamamoto; S. Ogata. 3-D thermodynamic analysis of superhydrophobic surfaces. J. colloid Interf. Sci. (2008) 326 (2), 471-477.

[55]T. Zhang; J. Wang; L. Chen; J. Zhai; Y. Song; L. Jiang. High-Temperature Wetting Transition on Micro- and Nanostructured Surfaces. Angew. Chem. (2011) 123, 23, 5311-5314.

[56]Y. Liu; X. Chen; J. Xin. Can superhydrophobic surfaces repel hot water? J. Mater. Chem. (2009) 19 31, 5602-5611.

[57]B. S. Kim; H. Lee,; S. Shin; G. Choi; and H. H. Cho. Interfacial wicking dynamics and its impact on critical heat flux of boiling heat transfer. Appl. Phys. Lett. (2014)105, 191601.

[58]N. Wang; Y. Zhao; L. Jiang. Low‐Cost, Thermoresponsive Wettability of Surfaces: Poly(N‐isopropylacrylamide)/Polystyrene Composite Films Prepared by Electrospinning. Macromol. Rapid Commun. (2008)29, 485-489.

[59]T. Sun; H. Liu; W. Song; X. Wang; L. Jiang; L. Li; D. Zhu. Responsive aligned carbon nanotubes. Angew. Chem. (2004) 116, 4663–4666.

[60]Y. Liu; H. Komatsuzaki; Z. Duan; S. Imai; and Y.Nishioka. Diffuser Micropump Structured with Extremely Flexible Diaphragm of 2-μm-thick Polyimide Film. Jpn. J. Appl. Phys. (2011) 50, 453-455.

[61]H. Komatsuzaki; K. Suzuki; Y. Liu; T. Kosugi; R. Ikoma; Y. nishioka. Flexible

Polyimide Micropump Fabricated Using Hot Embossing. Jpn. J. Appl. Phys. (2011) 50, 06GM09.

[62] P. C. Tsai; R. G. H. Lammertink; M. Wessling; D. Lohse. Evaporation-triggered wetting transition for water droplets upon hydrophobic microstructures. Phys. Rev. Lett. (2010) 104, 116102.

[63] S. Daniel; M. K. Chaudhury; J. C. Chen. Fast Drop Movements Resulting from the Phase Change on a Gradient Surface. Science (2001) 291, 633 –636.

[64] H. Linke; B.J. Alemán; L.D. Melling; M.J. Taormina; M.J. Francis; C.C. Dow-Hygelund; V. Narayanan; R.P. Taylor; A. Stout. Self-propelled Leidenfrost droplets. Phys. Rev. Lett. (2006) 96, 154502.

[65] C. Lv; C. Yang; P. Hao; F. He; Q. Zheng. Sliding of water droplets on microstructured hydrophobic surfaces. Langmuir (2010) 26(11), 8704–8708.

[66] Tak-Sing Wong and Chih-Ming Ho. Dependence of macroscopic wetting on nanoscopic surface textures. Langmuir (2009) 25, 12851-12854.

[67] C. Lv; Z. Wang; P. Wang; X. Tang. Photodegradable polyurethane self-assembled nanoparticles for photocontrollable release. Langmuir (2012) 28(25), 9387-9394.

[68] R. Tadmor. Line Energy and the Relation between Advancing,Receding, and Young Contact Angles. Langmuir (2004) 20, 7659-7664.

[69] Taegee Min and John Kim. Effects of hydrophobic surface on skin-friction drag. Physics of Fluids (2004) 16(7), L55-58

[70] C. Du, J. Wang, Z. Chen, D. Chen, Durable superhydrophobic and superoleophilic filter paper for oil–water separation prepared by a colloidaldeposition method, Appl. Surf. Sci. (2014) 313, 304–310.

[71] M.P. Sousa, J.F. Mano, Patterned superhydrophobic paper for microfluidic devices obtained by writing and printing, Cellulose (2013) 20, 2185–2190.

[72] C.-J. Chang, C.-F. Wang, J.-K. Chen, C.-C. Hsieh, P.-A. Chen, Fast formation ofhydrophilic and reactive polymer micropatterns by photocatalyticlithography method, Appl. Surf. Sci. (2013) 286, 280–286.

[73] Y.Y. Yan, N. Gao, W. Barthlott, Mimicking natural superhydrophobic surfaces

and grasping the wetting process: a review on recent progress in preparingsuperhydrophobic surfaces, Adv. Colloid Interface Sci. (2011) 169,80–105.

[74] T. Onda, S. Shibuichi, N. Satoh, K. Tsujii, Super-water-repellent fractal surfaces, Langmuir (1996) 12, 2125–2127.

[75] L. Jiang, Y. Zhao, J. Zhai, A lotus-leaf-like superhydrophobic surface: a porous microsphere/nanofiber composite film prepared by electro hydrodynamics, Angew. Chem. (2004) 116, 4438–4441.

[76] C.R. Crick, I.P. Parkin. Water droplet bouncing—a definition for superhydrophobic surfaces, Chem. Commun. (2011) 47, 12059–12061.

[77] R. Hensel, R. Helbig, S. Aland, H.G. Braun, A. Voigt, C. Neinhuis, C. Werner. Wetting resistance at its topographical limit: the benefit of mushroom and serif T structures, Langmuir (2013) 29, 1100–1112.

[78] Y. Lv, X. Yu, J. Jia, S.T. Tu, J. Yan, E. Dahlquist, Fabrication and characterization of superhydrophobic polypropylene hollow fiber membranes for carbondioxide absorption, Appl. Energy (2012) 90, 167–174.

[79] J.M. Lee, K.M. Bae, K.K. Jung, J.H. Jeong, J.S. Ko. Creation of microstructured surfaces using Cu–Ni composite electrodeposition and their application to superhydrophobic surfaces, Appl. Surf. Sci. (2014) 289, 14–20.

[80] Y. Wang, Y. Shi, L. Pan, M. Yang, L. Peng, S. Zong, Y. Shi, G. Yu. Multifunctional superhydrophobic surfaces templated from innately microstructured hydrogel matrix, Nano Lett. (2014) 14, 4803–4809.

[81] E. Celia, T. Darmanin, E.T. De Givenchy, S. Amigoni, F. Guittard. Recent advances in designing superhydrophobic surfaces, J. Colloid Interface Sci. (2013) 402, 1–18.

[82] B. Wang, J. Li, G. Wang, W. Liang, Y. Zhang, L. Shi, L. Guo, W. Liu. Methodology for robust superhydrophobic fabrics and sponges from in situ growth of transition metal/metal oxide nanocrystals with thiol modification and theirapplications in oil/water separation, ACS Appl. Mater. Interfaces (2013) 5, 1827–1839.

[83] K.M. Wisdom, J.A. Watson, X. Qu, F. Liu, G.S. Watson, C.H. Chen.

Self-cleaning of superhydrophobic surfaces by self-propelled jumping condensate, Proc.Nat. Acad. Sci. U. S. A. (2013) 110,7992–7997.

[84] G.D. Bixler, A. Theiss, B. Bhushan, S.C. Lee, Anti-fouling properties of microstructured surfaces bio-inspired by rice leaves and butterfly wings, J. Colloid Interface Sci. (2014) 419,114–133.

[85] L. Dellieu, M. Sarrazin, P. Simonis, O. Deparis, J.P. Vigneron, A two-in-one superhydrophobic and anti-reflective nanodevice in the grey cicada Cicada orni (Hemiptera), J. Appl. Phys. (2014) 116, 024701.

[86] E. Lepore, M. Giorcelli, C. Saggese, A. Tagliaferro, N. Pugno. Mimicking water striders' legs superhydrophobicity and buoyancy with cabbage leaves and nanotube carpets, J. Mater. Res. (2013) 28, 976–983.

[87] A. Milionis, D. Fragouli, L. Martiradonna, G.C. Anyfantis, P.D. Cozzoli, I.S. Bayer,A. Athanassiou. Spatially controlled surface energy traps on superhydrophobic surfaces, ACS Appl. Mater. Interfaces (2014) 6, 1036-1043.

[88] R. Fürstner, W. Barthlott, C. Neinhuis, P. Walzel, Wetting and self-cleaning properties of artificial superhydrophobic surfaces, Langmuir (2005) 21, 956–961.

[89] A. Lafuma, D. Quéré. Superhydrophobic states, Nat. Mater. (2003)2, 457–460.

[90] W. Li, A. Amirfazli, A thermodynamic approach for determining the contact angle hysteresis for superhydrophobic surfaces, J. Colloid Interface Sci. (2005) 292 (1), 195–201.

[91] A. Marmur, Wetting on hydrophobic rough surfaces: to be heterogeneous or not to be? Langmuir (2003) 19, 8343–8348.

[92]C. Lv; Z. Wang; P. Wang; X. Tang. Photodegradable polyurethane self-assembled nanoparticles for photo controllable release. Langmuir, (2012) 28(25), 9387-9394.

[93] Q.S. Zheng, Y. Yu, Z.H. Zhao, Effects of hydraulic pressure on the stability and transition of wetting modes of superhydrophobic surfaces, Langmuir (2005) 21, 12207–12212.

[94] M. J. Liu, Y. M. Zheng, J. Zhai, L. Jiang. Bioinspired Super-antiwetting

Interfaces with Special Liquid−Solid Adhesion. Acc. Chem. Res. (2010) 43, 368 – 377.

[95] T. L. Sun, L. Feng, X. F. Gao, L. Jiang. Bioinspired Surfaces with Special Wettability. Acc. Chem. Res. (2005) 38, 644 – 652.

[96] X. J. Feng, L. Jiang. Design and creation of superwetting/antiwetting surfaces. Adv.Mater. (2006) 18, 3063 – 3078.

[97] F. Xia, L. Jiang. Bio‐inspired, smart, multiscale interfacial materials. Adv. Mater. (2008) 20, 2842 – 2858;

[98] J. B. Boreyko, C. H. Chen. Self-propelled dropwise condensate on superhydrophobic surfaces. Phys. Rev. Lett. (2009) 103, 184051.

[99] M. Rein, Drop-surface interactions, Springer Verlag Wien. (2002) vol. 428.

[100] A. L. N. Moreira, A. S. Moita and M. R. Pan~ao, Prog. Advances and challenges in explaining fuel spray impingement: How much of single droplet impact research is useful? Energy Combust. Sci.(2010) 36, 554–580.

[101] S. H. Li, R. Furberg, M. S. Toprak, B. Palm, M. Muhammed. Nature‐Inspired Boiling Enhancement by Novel Nanostructured Macroporous Surfaces. Adv. Funct. Mater.(2008) 18, 2215 – 2220.

Scientific Contributions

Journal Paper

1) Profile Characterization and Temperature Effect on the Wettability of Microstructured Surfaces.
   Yuxuan Han, Yingwei Liu, Minami Kaneko, and Fumio Uchikoba.
   Journal of Surface Engineered Materials and Advanced Technology, (2018) 8, 83-94.
2) Bare Chip Mount of Neural Networks IC on MEMS Microrobot
   Yuxuan Han, Kazuki Sugita, Daisuke Tanaka, Minami Takato, Ken Saito, Fumio Uchikoba
   Proceedings of International Conference on Electronics Packaging 2016 FC1-3
3) High temperature Wetting Transition on Microstructrured Superhydrophobic Surface
   Yuxuan Han, Yingwei Liu, Minami Kaneko, and Fumio Uchikoba.
   (Under review)

Conferences

1) Profile characterization and temperature effect on wettability of microstructured surfaces **Yuxuan Han**, Yingwei Liu, Minami Takato and Fumio Uchikoba
   30th International Microprocesses and Nanotechnology Conference (MNC2017)
   November 6 - 9, 2017 / Ramada Plaza JeJu Hotel, JeJu, Korea.
2) Bare Chip Mount of Neural Networks IC on MEMS Microrobot
   Yuxuan Han，Sugita, K.，Tanaka, D.，Takato, M.，Saito, K.，Uchikoba,F.
   2016 International conference on Electronics Packaging，Sapporo，2016.4.20-2016.4.22
3) High temperature wettability on Microstructrured Superhydrophobic Surface
   Yingwei Liu, **Yuxuan Han**
   30th International Microprocesses and Nanotechnology Conference (MNC2017)
   November 6 - 9, 2017 / Ramada Plaza JeJu Hotel, JeJu, Korea.
4) How Temperture Affect Wettability on Microstructured Polyimide Surface

Yingwei Liu , **Yuxuan Han** , Zhengwei Yang , Yasushiro Nishioka
Conference of Photopolymer Science and Technology (CPST) ,June 25 - 28, 2017
International Conference Hall, Makuhari Messe, Chiba, Japan

5) SMA Actuator and Pulse-Type Hardware Neural Networks IC for Fast Walking Motion of Insect-Type MEMS Microrobot
Sugita, Kazuki ，Tanaka, Daisuke，Ono, Satoko，Chiba, Satohoro，Iwata, Kei，**Han Yuxuan**，Takato, Minami，Uchikoba, Fumio，Saito, Ken
2016 IEEE International Conference on Advanced Intelligent Mechatronics，Banff，2016.7.12-2016.7.15
6) Design of Electromagnetic Induction Type MEMS Motor withMultilayer Ceramic Three-Dimensional Coil
Takato, M. ，Yokozeki, Y.，Mishima, K.，**Han, Y.**，Saito,K.，Uchikoba, F.
2016 International Conference onElectronics Packaging ， Sapporo, ，2016.4.20-2016.4.22
7) Development of Electromagnetic MEMS Motor without Winding Wire and Application to Microrobot
Takato, Minami, Mishima, Kaito, **Han, Yuxuan**, Saito, Ken，Uchikoba, Fumio
2016 IEEE International Conference on Advanced Intelligent Mechatronics，Banff，2016.7.12-2016.7.15
8) Neural Networks IC for Locomotion Rhythm Generator Emulating Living Organism
Tanaka, D. ，Sugita, K.，**Han, Y.** ，Takato, M.，Uchikoba, F.，Saito, K.
2016 International Conference on Electronics Packaging (ICEP2017)，Sapporo，2016.4.20-2016.4.22
9) Development of Electromagnetic Induction Type MEMS Air Turbine Generator with Ball Bearing
Mishima, K. ，Yokozeki, Y.，**Han, Y.**，Takato, M.，Saito,K.，Uchikoba, F.
2016 International Conference on Electronics Packaging ， Sapporo ，2016.4.20-2016.4.22

Acknowledgement

This is a genuine pleasure to express my deep sense of thanks and gratitude to my supervisor and teachers.

Professor Fumio Uchikoba Thank him agree me as his student and give me this opportunity to study in his lab. For his guidance and support, I could insist on and complete the Ph.D. For his kindly concern and encouragement, I enjoyed the studying life in Japan.

Assistant Professor Minami Kaneko & Associate Professor Ken Saito To help me contact other professors using the experiment equipment, give me training, and give much more support and help on studying.

Professor Yoshio Aoki & Professor Hiroshi Matsuda Thank them give me many suggestions that help me improve my thesis.

Professor Yoshito Ashizawa Thank him give me training and support on the contact angle measurement which is the most important device and I used lot in my studies.

Professor Nobuyuki Iwata Thank him for his support on AFM scanning.

Natural Science Foundation of China To support on a part of the Si fabrication in financial.

My parents and family Thank them give me support and encouragement.